


RESEARCH ARTICLE | MARCH 27 2023

Parametric investigation of azimuthal instabilities and electron transport in a radial-azimuthal $E \times B$ plasma configuration ^{EP}

M. Reza  ; F. Faraji ; A. Knoll

 Check for updates

Journal of Applied Physics 133, 123301 (2023)

<https://doi.org/10.1063/5.0138223>


View
Online


Export
Citation

 CrossMark

Articles You May Be Interested In

Conditions of appearance and dynamics of the modified two-stream instability in $E \times B$ discharges

Physics of Plasmas (April 2021)

Evolution of the electron cyclotron drift instability in two-dimensions

Physics of Plasmas (August 2018)

Influence of the axial oscillations on the electron cyclotron drift instability and electron transport in Hall thrusters

Physics of Plasmas (April 2023)



Time to get excited.
Lock-in Amplifiers – from DC to 8.5 GHz

[Find out more](#)

 Zurich
Instruments

Parametric investigation of azimuthal instabilities and electron transport in a radial-azimuthal $E \times B$ plasma configuration



Cite as: J. Appl. Phys. 133, 123301 (2023); doi: 10.1063/5.0138223

Submitted: 9 December 2022 · Accepted: 8 March 2023 ·

Published Online: 27 March 2023



View Online



Export Citation



CrossMark

M. Reza,^{a)} F. Faraji, and A. Knoll

AFFILIATIONS

Plasma Propulsion Laboratory, Department of Aeronautics, Imperial College London, Exhibition Road, London, SW7 2AZ, United Kingdom

^{a)}Author to whom correspondence should be addressed: m.reza20@imperial.ac.uk

ABSTRACT

Partially magnetized low-temperature plasmas (LTP) in an $E \times B$ configuration, where the applied magnetic field is perpendicular to the self-consistent electric field, have become increasingly relevant in industrial applications. Hall thrusters, a type of electrostatic plasma propulsion, are one of the main LTP technologies whose advancement is hindered by the not-fully-understood underlying physics of operation, particularly, with respect to the plasma instabilities and the associated electron cross field transport. The development of Hall thrusters with unconventional magnetic field topologies has imposed further questions regarding the instabilities' characteristics and the electrons' dynamics in these modern cross field configurations. Accordingly, we present in this effort a detailed parametric study of the influence of three factors on the plasma processes in the radial-azimuthal coordinates of a Hall thruster, namely, the magnetic field gradient, secondary electron emission, and plasma number density. The studies are carried out using the reduced-order particle-in-cell code developed by the authors. The setup of the radial-azimuthal simulations largely follows a well-defined benchmark case from the literature in which the magnetic field is oriented along the radius, and a constant axial electric field is applied perpendicular to the simulation plane. The salient finding from our investigations is that, in the studied cases corresponding to elevated plasma densities, a long-wavelength azimuthal mode with the frequency of about 1 MHz is developed. Moreover, in the presence of strong magnetic field gradients, this mode results from an inverse energy cascade and induces a significant electron cross field transport as well as a notable heating of the ions.

© 2023 Author(s). All article content, except where otherwise noted, is licensed under a Creative Commons Attribution (CC BY) license (<http://creativecommons.org/licenses/by/4.0/>). <https://doi.org/10.1063/5.0138223>

I. INTRODUCTION

Low-temperature plasma technologies in which a partially magnetized plasma is subject to perpendicular electric and magnetic fields, such as the magnetrons for material processing and Hall thruster for spacecraft plasma propulsion, are today of high interest from both the applied and scientific perspectives. Particularly in case of the Hall thrusters, they are currently considered as optimal solutions for a variety of next-generation space mission scenarios due to their relatively higher propulsive metrics, easier manufacturing, and higher versatility of operation compared to other electrostatic electric propulsion solutions. Moreover, the rich underlying physics of plasma in Hall thrusters has made them a subject of active research in the last few decades. The $E \times B$

plasma configuration of these thrusters and the consequent large gradients and anisotropies in the plasma lead to a wide range of instabilities and oscillations developing across a broad spectrum of spatial and temporal scales. These processes are demonstrated to significantly affect the dynamics of the plasma species, in particular, the electrons.¹ The modification of the electrons' dynamics by the instabilities can affect the global performance and stability of the plasma discharge and, hence, the operation of the Hall thrusters. This coupling between the underlying physics and the operational behavior of Hall thrusters provides the academic research into the plasma phenomena in these devices an important applied significance since the resulting insights enable the development of high-performance, optimized devices, and their reliable in-space applications.

Establishing clear links between the plasma instabilities and the operation of Hall thrusters requires a comprehensive understanding of the nature and characteristics of the instabilities in each operating condition, characterizing the nonlinear interactions among the instability modes, and identifying the mechanisms by which these instabilities influence the electrons' dynamics during various phases of their evolution and across the plasma conditions. In this regard, the three-dimensional, multiscale nature of the instabilities in Hall thrusters' plasma, which has become increasingly evident by the mounting body of research,² poses a major challenge for progress in this direction.

Nevertheless, in the absence of high-fidelity 3D plasma simulations of Hall thrusters, the investigation of the above aspects has been pursued in various 2D configurations and has led to valuable insights into the dominant instability modes, their interplays, and their contributions to electrons' cross field transport. In this regard, the study of the impact of plasma-wall interactions and radial plasma gradients on the instabilities and the resulting electrons' transport in the radial-azimuthal coordinates is a growing area of interest. Over the past years, the main subjects of research have been the excitation and evolution of the electron cyclotron drift instability (ECDI),^{3,4} the effect of the plasma-wall interactions on this instability,^{5,6} and the role of the ECDI in electron transport.⁴ In particular, the nonlinear evolution of the ECDI and the impact of the radial direction on the dynamics of azimuthal instabilities is studied in Ref. 3, in which the authors observed that the instabilities evolve toward larger azimuthal wavelengths and, at the later stages of the nonlinear evolution, the excitation of the so-called "modified two-stream instability (MTSI)" intensifies this inverse energy cascade. The evolution of the instabilities toward longer wavelength modes has been also evidenced in Ref. 7.

Regarding the impact of the MTSI on the plasma properties, the simulations of Refs. 3 and 7 showed that, because of its wave-vector component along the magnetic field, the instability causes strong heating of the electrons in the radial direction. They also observed that the MTSI plays a significant role in the electrons' axial transport. In fact, in Ref. 7, the authors distinguished the contributions of the ECDI and the MTSI to transport using a dynamic mode decomposition (DMD) analysis and concluded that the MTSI, when present, has the dominant contribution.

The interactions between the ECDI and the secondary electrons emitted from the walls, together with their combined roles in "anomalous" cross field transport of electrons, have been studied in Ref. 5. From their kinetic PIC simulations, the authors showed that, in the presence of high secondary electron emission (SEE) rates, the "beam-plasma" instability is excited which induces very large axial electron currents. In Ref. 6, the individual effect of the SEE on the sheath characteristics and the electrons' transport was investigated by performing a wide-range parametric study. The authors observed that increasing the SEE yield coefficient from 0 to 1 enhances the near-wall cross field mobility of the electrons by a factor of 2 while decreasing the mobility in the bulk due to the cooling effect of secondary emitted electrons.⁶ The results of Ref. 6 complemented prior investigations of the role of SEE in the electrons' dynamics and mobility in $E \times B$ configurations^{8–11} by extending the analyses to a 2D radial-azimuthal configuration. In addition, in Ref. 12, the authors used a cylindrical 2D

radial-azimuthal simulation and showed that an enhancement of the electron cross field mobility can occur due the presence of a high-frequency sheath instability in the space-charge-saturated (SCS) regime. They demonstrated that the instability arises from the negative differential resistance in the I - V characteristics of the wall in this regime.¹²

Finally, noting the recent development of high-power Hall thrusters with the so-called "shielding" magnetic field topologies¹³ designed to address the life-limiting issue of the erosion of the thrusters' channel, some limited research has been carried out to investigate the instabilities' characteristics and the electrons' transport in these unconventional field configurations. In this respect, the authors in Ref. 14 numerically solved the electrostatic dispersion relation of a homogeneous, unbounded plasma with the conditions representative of the near-plume region of a magnetically shielded Hall thruster obtained from 2D axial-radial multifluid PIC simulations. They noticed the presence of the MTSI with the fastest growing mode occurring close to the front magnetic poles of the thruster.¹⁴ As according to Ref. 15, the MTSI can heat up the ions perpendicular to the magnetic field almost to the same extent as it heats up the electrons parallel to field lines, the authors concluded that this could have a significant implication on the energy deposition on and sputtering of the magnetic poles.¹⁴

Most recently, the impact of the magnetic field gradients and curvature on the plasma is analyzed using a 1D radial PIC simulation in Ref. 16. In this publication, the authors performed simulations with various magnetic field curvatures and showed that the electron distribution function becomes more isotropic, and the tail of the electrons' distribution function is greatly replenished.¹⁶ They also observed a concentrating effect in cases with concave magnetic field curvatures such as those encountered inside the channel of magnetically shielded Hall thrusters. It was noticed that the density in the center of the domain becomes higher than the case with a constant radial magnetic field.¹⁶

Considering the above overview, the aim of the present article is to provide a comprehensive evaluation of the influence of various physical factors on the dynamics of the azimuthal instabilities and the consequent electrons' cross field mobility using high-fidelity reduced-order kinetic simulations. The simulations are performed for relatively long timescales so as to cast light as well on the long-term evolution and interactions of the instabilities. The use of our reduced-order PIC code, introduced and verified in Refs. 17 and 18, serves as an essential enabler for this effort due to its remarkably lower computational cost compared to the conventional full-2D PIC codes and its high predictions' accuracy, which is on a par with the traditional 2D codes. The factors whose influence we analyze in this paper are the magnetic field gradient, the secondary electron emission, and the plasma number density. As such, the analyses and discussions presented in this article are meant to expand the knowledge available in the literature concerning the radial-azimuthal physics of Hall thrusters and similar $E \times B$ discharges.

To perform the physical parametric studies in a simulation setup that is rigorously defined and is widely accepted within the $E \times B$ plasmas research community, we adopted, as the baseline setup, the one used for the radial-azimuthal kinetic code benchmarking activity.¹⁹ Accordingly, the simulations in this work allow

us to build upon the well-known results from the benchmark and to evaluate the variations in the observed behaviors due to each of the abovementioned three physical factors. Consequently, it is worth briefly describing the main physics that has been reported in the benchmark publication.¹⁹ In this regard, the authors observed a cyclic quasi-steady evolution of the plasma discharge after an initial transient. During this transient, the ECDC and MTSI modes were developed. For detailed information about these instability modes, including the derivation and analysis of their dispersion relations, interested readers are referred to the existing literature, such as Refs. 3, 7, 20–23, and the references therein. The nonlinear interactions between these instabilities were observed to lead to the periodic growth and damping of the two modes. When the MTSI modes were strongest, the radial electron temperature was seen to be at a local maximum. The damping of the MTSI resulted in a reduction of the radial electron temperature. When the radial electron temperature reached a local minimum, it was demonstrated that the ECDC becomes dominant.¹⁹ It was also emphasized in Ref. 19 that the periodic oscillations in the radial electron temperature are reflected in the time evolution of the plasma density, which is due to the coupling that the imposed ionization source introduces between these two parameters in the benchmark's simulation case.

Before proceeding further, the extensive nature of this article warrants providing an overview of the paper's organization at this point. In this regard, in Sec. II, we provide an overview of the reduced-order quasi-2D particle-in-cell code that is developed at Imperial Plasma Propulsion Laboratory (IPPL). The simulation setup and conditions are reviewed in Sec. III. We present in Sec. IV the results of our parametric studies. We begin by discussing the effects of the magnetic field gradients in Sec. IV A. Next, in Sec. IV B, we assess the influence of the SEE and, finally, in Sec. IV C, we evaluate the effects of the plasma number density. In Sec. IV, the effects of each physical factor on the plasma discharge are analyzed in terms of the variation in (1) the distribution of the macroscopic plasma properties, (2) the characteristics of the azimuthal instabilities, and (3) the electrons' transport. Concerning the azimuthal instabilities, in particular, we have characterized the observed fluctuations using spatial and temporal spectral analyses. The main findings and insights from this effort are summarized in Sec. V.

II. OVERVIEW OF THE REDUCED-ORDER IPPL-Q2D PIC CODE

IPPL-Q2D is a quasi-2D electrostatic explicit kinetic code based on the generalized reduced-order PIC scheme.¹⁷ The reduced-order PIC is an innovative plasma simulation technique, devised by the authors, to tackle the computational cost issue of the conventional PIC schemes. It is predicated on a dimensionality-reduction approach for the decomposition of multi-dimensional Poisson's equation into a system of coupled 1D ODEs. The reduced-order scheme also features a decomposition of the domain into multiple "regions."¹⁷ Within each region, a fine discretization of the simulation dimensions is carried out using custom 1D cells, which enables resolving the variations of the plasma properties separately along each simulation

coordinate.¹⁸ Accordingly, for a 2D simulation case, the number of required computational cells and, hence, the total number of macroparticles can be reduced from $O(N^2)$ to $O(N)$, with N being the number of cells along each simulation direction. This translates into significantly lower computational resource demand of the quasi-2D PIC compared to the traditional full-2D codes.¹⁷ The detailed explanation of the reduced-order PIC scheme and its underlying dimensionality-reduction formulation can be found in Refs. 17 and 18.

The overall structure and the algorithmic implementations of IPPL-Q2D are introduced in Refs. 17 and 18. The reduced-order quasi-2D code is verified extensively in our previous works against the well-defined axial-azimuthal^{17,24} and radial-azimuthal¹⁸ benchmark cases available in the literature. Particularly relevant to the present paper, the verifications of IPPL-Q2D in the radial-azimuthal simulation setup of the benchmark showed that a 50-region quasi-2D simulation, which offers a factor of 5 speed-up with respect to a full-2D simulation, provides high-fidelity predictions of the underlying physical processes and the plasma properties' distribution that compare well with the full-2D results.¹⁸ Consequently, the simulations in this work are carried out using this approximation order of the 2D problem.

For the investigation of the effects of SEE, we have used the wall-interaction module of IPPL-Q2D. The wall-interaction module is described in Ref. 25, which also reports some of its verification results. In this work, we have used the linear SEE model from the wall-interaction module, which is further explained in Sec. IV B.

III. DESCRIPTION OF THE SIMULATION SETUP AND CONDITIONS

The setup and conditions of the simulations performed in this effort are overall based on the 2D radial-azimuthal benchmark case by Villafana *et al.*¹⁹ In any case, certain modifications are introduced in the baseline benchmark setup to enable the investigation of the effect(s) of each specific physical aspect mentioned in Sec. I. We highlight these modifications in the following after providing an overview of the baseline setup.

The simulation domain is a 2D $x-z$ Cartesian plane, representative of a radial-azimuthal section of a Hall thruster. The x -coordinate is along the radial direction, and the z -coordinate represents the azimuthal direction. The y axis is directed along the axial direction. The domain is 1.28-cm long along both the radial and azimuthal directions. All simulations are collisionless and are run for 30 μ s. A constant axial electric field is applied in all studied cases. Table I presents the values of the main computational and physical parameters used for the simulations.

At the beginning of the simulations, the electrons and ions are sampled from a Maxwellian distribution at 10 and 0.5 eV, respectively, and are loaded uniformly throughout the domain at exactly the same positions. In order to limit the growth of the azimuthal waves and the particles' energy in the simulations,²⁶ the approach of Ref. 19 is pursued, and a virtual axial extent with the length of $L_y = 1$ cm is considered. The particles crossing a domain's boundary along the axial direction are resampled from their initial Maxwellian distribution and are re-injected onto the

TABLE I. Summary of the computational and physical parameters used for the radial-azimuthal quasi-2D simulations.

Parameter	Value (unit)
Computational parameters	
Domain length ($L_x = L_z$)	1.28 (cm)
Virtual axial length (L_y)	1 (cm)
Cell size ($\Delta x = \Delta z$)	50 (μm)
Number of cells in each direction ($N_i = N_k$)	256
Time step (t_s)	1.5×10^{-11} (s)
Total simulated duration (t_{sim})	30 (μs)
Initial number of macroparticles per cell (N_{ppc})	100
Physical parameters	
Initial plasma density ($n_{i,0}$)	5×10^{16} (m^{-3})
Initial electron temperature ($T_{e,0}$)	10 (eV)
Initial ion temperature ($T_{i,0}$)	0.5 (eV)
Axial electric field (E_y)	10 000 (V m^{-1})
Radial magnetic field intensity at the mid-radial plane (B_x)	0.02 (T)
Electric potential at the walls (ϕ_w)	0 (V)

simulation plane, maintaining their azimuthal and radial positions.

In all simulation cases, a zero-volt Dirichlet boundary condition is used for the electric potential at the walls. It is noteworthy that, in a Cartesian radial-azimuthal configuration, the symmetry of the simulation domain results in the absence of any net electron and ion current reaching the radial boundaries, which implies that the electrically floating boundary condition is automatically satisfied at the walls.⁶ Hence, the adopted Dirichlet boundary condition in this study is reasonably well representative of the more realistic floating wall condition in modern Hall thrusters that feature a dielectric wall material. A periodic boundary condition is considered in the potential solver for the nodes at the two azimuthal ends of the domain. Moreover, particles that exit the domain along the azimuth from one side are re-introduced into the domain from the opposite side.

In order to compensate for the flux of particles lost to the walls, the approach of the radial-azimuthal benchmark¹⁹ is adopted, and an ionization source is imposed. As described in more detail in Ref. 19, the ionization source is uniform in the azimuthal (z) direction and has a cosine distribution along the radius (x), extending from $x = 0.09$ cm to $x = 1.19$ cm. The peak of the ionization source (S_0) is nominally $8.9 \times 10^{22} \text{ m}^{-3} \text{ s}^{-1}$, which corresponds to an axial ion current density of 100 A m^{-2} . The electron-ion pairs injected at each time step due to the ionization source are sampled from a Maxwellian at the respective initial temperature of each species.

We underline that adopting an approach to compensate for the radial flux of particles is a necessity for achieving steady-state condition in all simulations studying the plasma-wall interactions in 1D and 2D which do not self-consistently resolve the axial fluxes of the plasma species. In this regard, the adoption of an ionization source is one of the proposed approaches in the literature,^{4,19,27}

which, as explained in Sec. I, results in the simulations reaching a quasi-steady state.

Concerning the aspects of the simulation setup specific to each investigated case in Sec. IV, for the simulations in Sec. IV A, which are dedicated to the study of the effects of the magnetic field gradients, the field intensity has a distribution along the radial coordinate with the magnitude at the mid-radial plane being equal to 20 mT. In all other simulated cases, the magnetic field has only a constant radial component with the same magnitude of 20 mT.

In Sec. IV B, which is related to the study of the influence of SEE, the electrons' radial boundary condition is different with respect to the other simulations carried out. Indeed, whereas electrons hitting a wall are, in general, removed from the simulation, the secondary electron emission is accounted for using a linear model for the simulations of Sec. IV B. The secondary emitted electrons are sampled from a Maxwellian at the assumed temperature of 2 eV. Regarding the ions, they are always removed from the simulation in all studied cases if they cross a radial boundary.

Finally, in Sec. IV C, where we study the effects of the plasma number density (or, equivalently, the axial current density), the nominal peak of the ionization source (S_0) is multiplied by a factor α corresponding to the ratio of the imposed current density for each case to the nominal one (100 A m^{-2}). Accordingly, the initial plasma density ($n_{i,0}$) was scaled by the same factor, whereas the cells' size (Δx and Δz) and the simulations' time step were scaled by $1/\sqrt{\alpha}$.

IV. EFFECTS OF RADIAL MAGNETIC FIELD GRADIENTS, SEE, AND CURRENT DENSITY ON THE RADIAL-AZIMUTHAL PLASMA PHENOMENA

In this section, we present and discuss the results from our 50-region quasi-2D simulations aimed at studying the individual influence(s) on the radial-azimuthal dynamics of the plasma due to each of following factors: (1) radial gradients in the magnetic field, (2) secondary electron emission, and (3) plasma number density.

A. The effect of radial gradients in the magnetic field

Figure 1 shows the radial profiles of the radial (B_x) and axial (B_y) components of the magnetic field, as well as the radial distributions of the magnetic field intensity (B) and the angle (θ) between the magnetic field lines and the radial coordinate (x) for three studied magnetic field configurations. Moreover, Fig. 1(e) presents a 2D schematic of the adopted magnetic field topology in this work. Referring to plot (a) in Fig. 1, among the three studied magnetic field configurations, Config. 1 corresponds to that of the baseline benchmark setup. Config. 2 has a convex radial profile of B_x , with the magnitude of the radial component increasing from $B_x = 0$ at the walls to the maximum value at the mid-radial location. Config. 3 has instead a concave B_x radial profile, with the maximum B_x occurring at the two radial ends of the domain. Magnetic field configurations 2 and 3 are representative of the "magnetic-shielding" topology. In this respect, it is seen in Fig. 1(e) that Config. 2 resembles the shielding configuration inside a Hall thruster's discharge channel, whereas Config. 3 corresponds to the field topology slightly outside the channel and within the "magnetic lens."²⁸

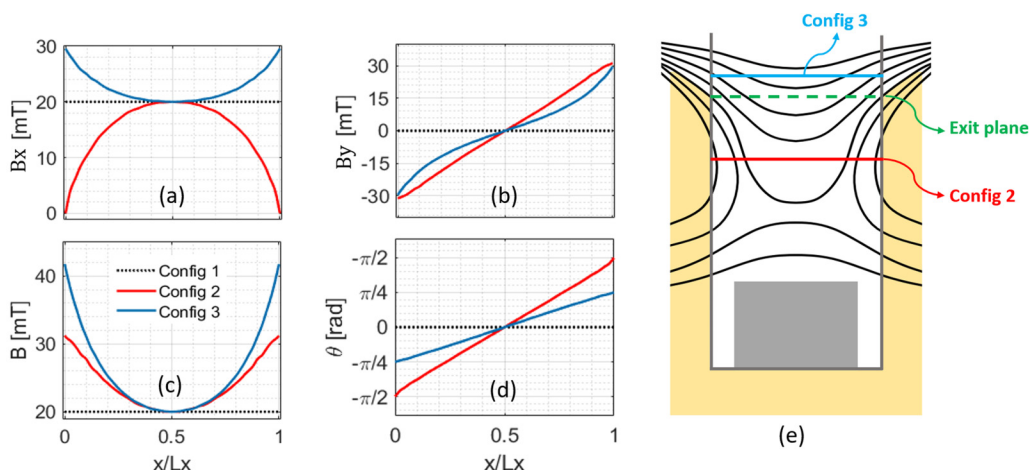


FIG. 1. Radial profiles of the studied magnetic field configurations: (a) radial component (B_x), (b) axial component (B_y), (c) magnetic field intensity (B), and (d) the angle between the tangent to the magnetic field lines and the x -coordinate. In plot (e), a schematic of the adopted field topology and the cross sections corresponding to Configs. 2 and 3 are shown.

From plot (c) in Fig. 1, it is noticed that the gradient in the magnetic field intensity is larger for Config. 3, which is expected to result in a more pronounced magnetic mirror effect due to a larger ∇B force, i.e., the force due to the gradient in the magnetic field. In addition, plot (b) in Fig. 1 shows that B_y varies from -30 to 30 mT from one wall to the other in Configs. 1 and 2 and becomes zero at the mid-radial plane. Finally, looking at plot (d) in Fig. 1, it is evident that, in Config. 2, the magnetic field lines are parallel to the walls at the radial extremes of the domain, which, as will be demonstrated later, results in a notably reduced flux of particles to the walls.

We start presenting the results from various B-Config simulations with the radial distributions of the time-averaged plasma properties, ion number density (n_i), electron temperature (T_e), and ion temperature (T_i), in Fig. 2. Looking at plot (a) in this figure, it

is observed that, for Configs. 2 and 3, n_i is much higher in the center of the domain compared to Config. 1. This higher density points to the confinement of the plasma by the magnetic field as the radial flux of plasma species is reduced in Configs. 2 and 3. In this respect, as the ∇B force is larger in Config. 3 [Fig. 1(c)], the plasma is more concentrated in the center in this case compared to Config. 2. Similar observations are also reported in Ref. 16 from 1D radial simulations in which the effect of the magnetic field curvature on the radial distribution of the plasma properties was investigated.

Referring now to Fig. 2(b), we notice that T_e is relatively the same for Config. 2 compared to Config. 1, but it is much lower for Config. 3. As it will be shown in the following, the notably lower time-averaged T_e for Config. 3 is due to the absence of the ECDCI modes in this magnetic field configuration. Nonetheless,

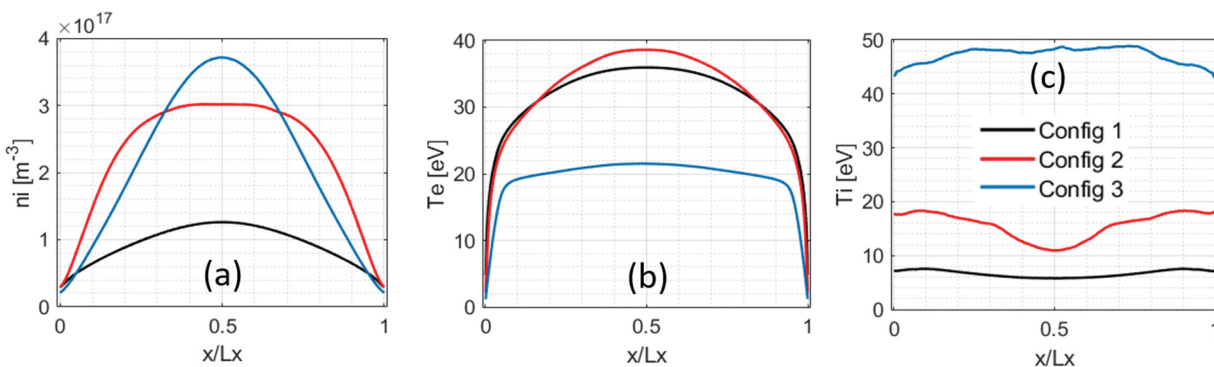


FIG. 2. Radial profiles of plasma properties averaged over $25\text{--}30\ \mu\text{s}$ from the simulations with various magnetic field configurations: (a) ion number density, (b) electron temperature, and (c) ion temperature.

Downloaded from http://pubs.aip.org/jap/article-pdf/doi/10.1063/5.0138223/16788652/123301_1_online.pdf

from plot (c) in Fig. 2, it is seen that a significant ion heating has occurred in Config. 3. Indeed, the time-averaged T_i profile for Config. 3 shows notably higher values across the radial extent of the domain. T_i is also higher in Config. 2 compared to Config. 1, which implies some degree of ion heating in this configuration as well but clearly less significant than that in Config. 3.

Figure 3 shows the time evolution of the ion number density [plot (a)], electron temperature [plot (b)], average ions' kinetic energy [plot (c)], and the electrons' axial mobility [plot (d)], for the three magnetic field configurations. The ions' kinetic energy and the electrons' axial mobility are calculated using Eqs. (1) and (2), respectively. In Eq. (1), E_i is the ions' average kinetic energy in eV, M_i is the ion mass, e is the unit charge, N_i is the total number of ion macroparticles, and $\mathbf{v}_{i,n}$ is the velocity vector of the n th ion macroparticle. In Eq. (2), μ is the electrons' axial mobility, \mathbf{v}_{ye} is the axial electron velocity, E_y is the axial electric field, and N_e is the total number of electron macroparticles,

$$E_i = \frac{1}{2} \left(\frac{M_i}{N_i e} \right) \sum_{n=1}^{N_i} (\mathbf{v}_{i,n} \cdot \mathbf{v}_{i,n}), \quad (1)$$

$$\mu = \left| \frac{\sum_{n=1}^{N_e} \mathbf{v}_{ye}}{N_e E_y} \right|. \quad (2)$$

Referring to Fig. 3, it is observed that the fluctuations in various plasma parameters are of much higher amplitude and lower frequency for Config. 3 with respect to the other two magnetic field configurations. Moreover, the mean ions' kinetic energy and electrons' axial mobility is also higher for Config. 3 compared to Configs. 1 and 2. In Config. 2, the time evolution plots of ions' energy and electrons' mobility show higher-frequency,

lower-amplitude oscillations, and a lower time-averaged E_i and μ compared to Config. 3. The mean E_i and μ for Configs. 2 and 3 are both larger than the corresponding values for Config. 1.

The different temporal behaviors of the plasma parameters in Fig. 3 suggest that, among the three magnetic configurations, there are notable variations in the underlying physical mechanisms and interactions. To illustrate this point, we first refer to Fig. 4, in which we show, for each magnetic configuration, the 2D snapshots of various plasma properties at an instance of time corresponding to a local maximum in radial electron temperature (T_{ex}).

As described in Sec. I, in the benchmark's simulation setup, which is identical to Config. 1, it has been observed that, when the radial electron temperature is maximum, the MTSI is fully formed and is dominant.^{18,19} In this regard, the plots on the first row of Fig. 4, which correspond to Config. 1, are reminiscent of the results from the benchmark¹⁹ and our previous work,¹⁸ with the radial and azimuthal wavenumbers of the MTSI being particularly observable in the axial current density (J_{ey}) distribution. However, the 2D snapshots for Configs. 2 and 3 show notably different structures with respect to each other and also compared to Config. 1. Of course, in both configurations, MTSI-like patterns can be noticed, but the distributions and amplitudes are quite dissimilar.

Second, in Fig. 5, we have plotted for each magnetic configuration the 2D snapshots of the electron axial current density over one period of the discharge evolution (T). The video of the cyclic behavior shown in Fig. 5 for the three B-Configs. is available in Ref. 29, which more clearly visualizes the involved dynamics in each case. Looking at the evolution of J_{ey} for Config. 1, the observed periodic behavior is similar to that reported in Refs. 18 and 19. Indeed, at $t = t_0$, the MTSI is dominant. This instability starts to mitigate at $t_0 + \frac{T}{4}$, and the ECDI modes become eventually dominant at $t_0 + \frac{T}{2}$. The nonlinear interactions between MTSI and

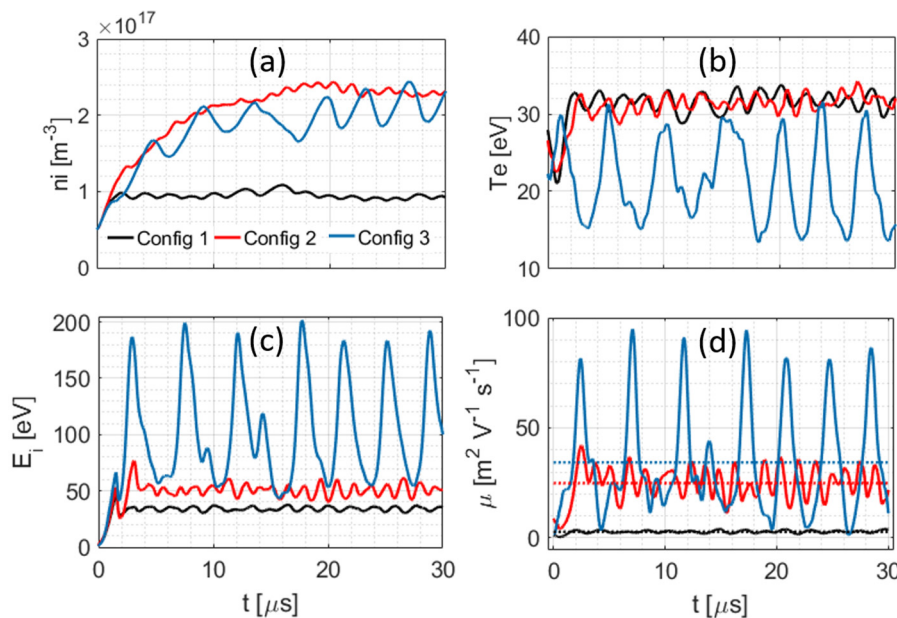


FIG. 3. Time evolution of various plasma parameters from the simulations with various magnetic field configurations: (a) ion number density, (b) electron temperature, (c) average ions' kinetic energy, and (d) average electron's axial mobility. The horizontal dashed lines in plot (d) show the time-averaged mobility values.

Downloaded from http://pubs.aip.org/aip/jap/article-pdf/doi/10.1063/5.0138223/16788652/123301_1_online.pdf

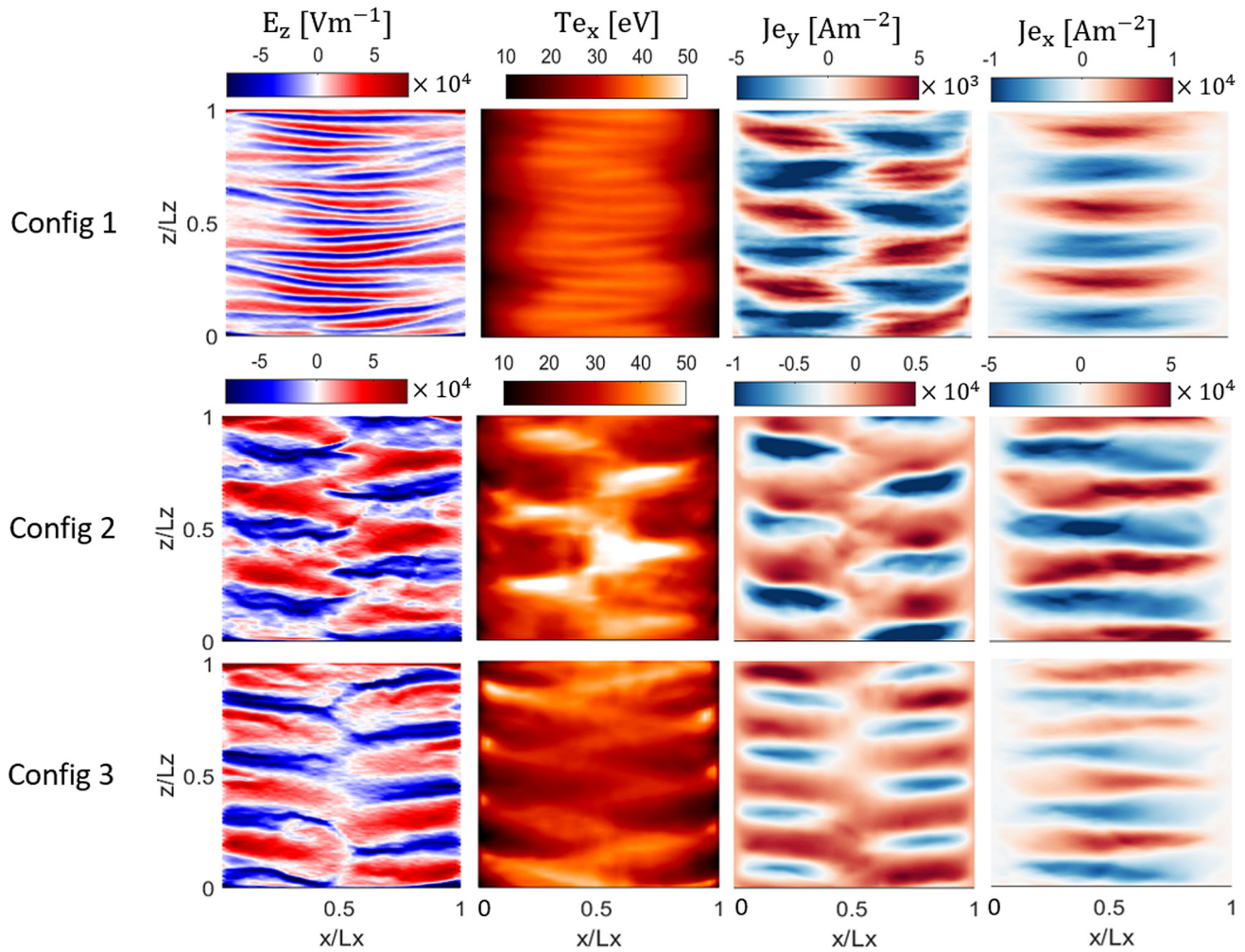


FIG. 4. Comparison of the 2D snapshots of plasma properties at the time of local maximum of radial electron temperature for various magnetic field configurations. The columns, from left to right, represent the azimuthal electric field (E_z), radial electron temperature (T_{ex}), and axial and radial electron current densities (J_{ey} and J_{ex}).

ECDI¹⁹ leads to the disruption of the ECDI waves and the growth of the MTSI waves at $t_0 + \frac{3T}{4}$. Finally, the MTSI becomes fully formed and dominant again at $t = T$, and the cycle repeats. This described interaction between the ECDI and the MTSI modes is also visible in Fig. 6(a), which shows the time evolution of the azimuthal wavenumber content of the electric field fluctuations along the azimuth for Config. 1.

In Configs. 2 and 3, the same cyclic growth and damping of the MTSI is seen in Fig. 5. However, the damping of the MTSI modes in the latter magnetic configuration is noticed from Fig. 6(b) to be associated with an inverse energy cascade that leads to the formation of a long-wavelength mode. The large structure in Config. 3 is observed in Fig. 5 (bottom row) to break away at $t = t_0 + \frac{3T}{4}$, when the lower-wavelength MTSI-like modes start to grow and then become again dominant at $t = T$.

To further elaborate on the characteristics of the observed wave modes in Figs. 4–6, we have shown, in Fig. 7, the spatiotemporally averaged 1D spatial FFT plots of the azimuthal electric field signal from the B-Config simulations in three time intervals along the simulations. Moreover, we have plotted, in Fig. 8, the frequency spectra of the azimuthal electric field signal from various B-Config simulations.

The plots in Fig. 7 are obtained using the same approach detailed in Refs. 3 and 19. The horizontal axis of the spatial FFT plots is the normalized azimuthal wavenumber, k_z/k_0 , where k_0 is the fundamental resonance wavenumber of the ECDI defined as $k_0 = \frac{\Omega_{ce}}{v_{de}}$.¹⁹ In the relation for k_0 , Ω_{ce} is the electron cyclotron frequency, and v_{de} is the electrons' azimuthal drift velocity. To calculate Ω_{ce} for Configs. 2 and 3, in which the magnetic field intensity varies along the radius, we have used the B value at the mid radial

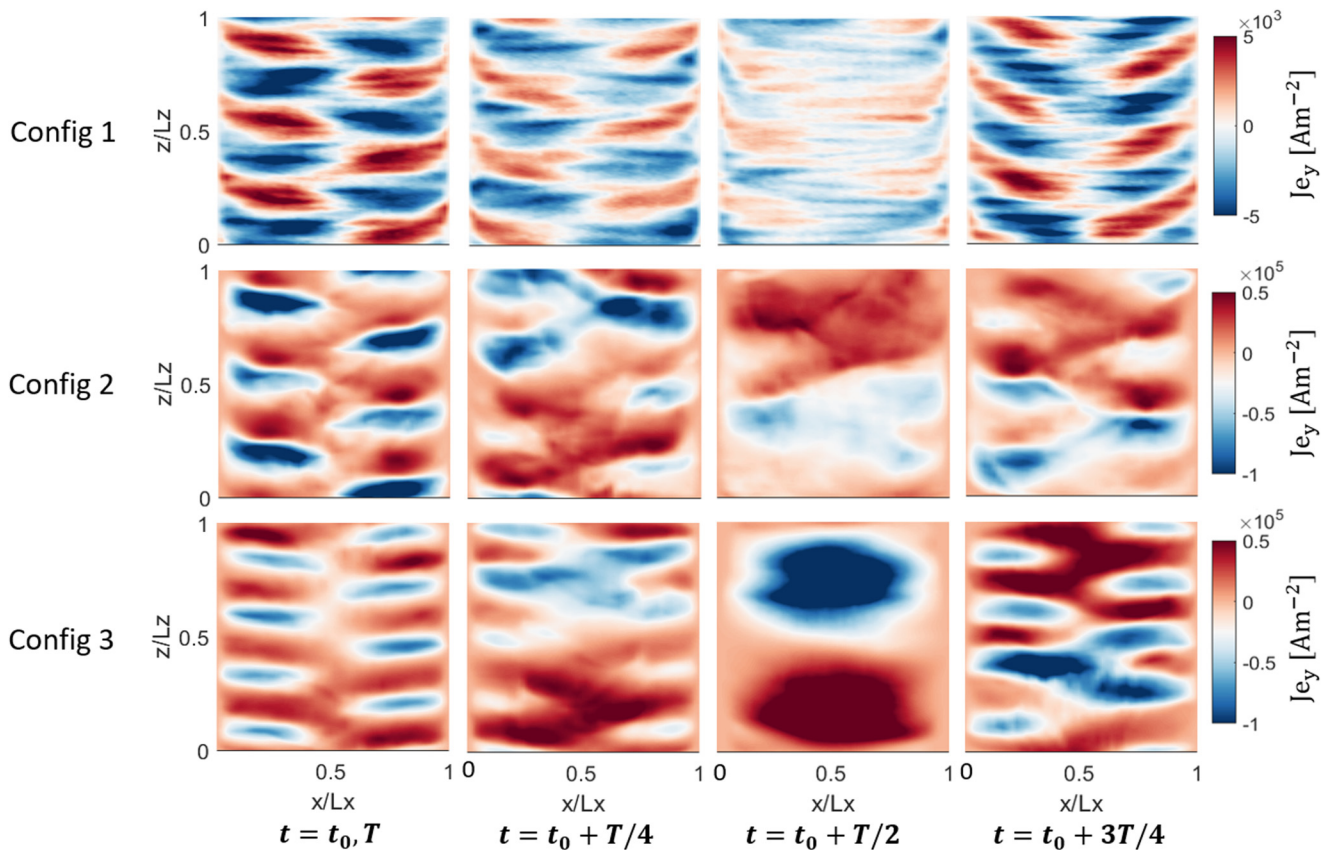


FIG. 5. 2D snapshots of the axial electron current density at four different moments through the discharge evolution cycle for each magnetic field configuration. T represents the period of the cycle, which is different for each case.

location, i.e., 20 mT, so that k_0 in these two cases is consistent with its value for Config. 1.

Referring to Fig. 7, we first notice that, for Config. 1, the first and second harmonics of the ECDI at $\frac{k_z}{k_0} \sim 1$ and $\frac{k_z}{k_0} \sim 2$, respectively, as well as the MTSI mode at $\frac{k_z}{k_0} \sim 0.2$ are present in all time intervals. The frequency of the first ECDI harmonic from Fig. 8 is

5.4 MHz, whereas the second harmonic has a frequency in the range of 10–11 MHz. The frequency of the MTSI mode in Config. 1 is 1.2 MHz.

For Configs. 2 and 3, we see from Figs. 7 and 8 that the ECDI modes did not excite. For Config. 2, we notice the presence of the first and second harmonics of the MTSI, with the first harmonic

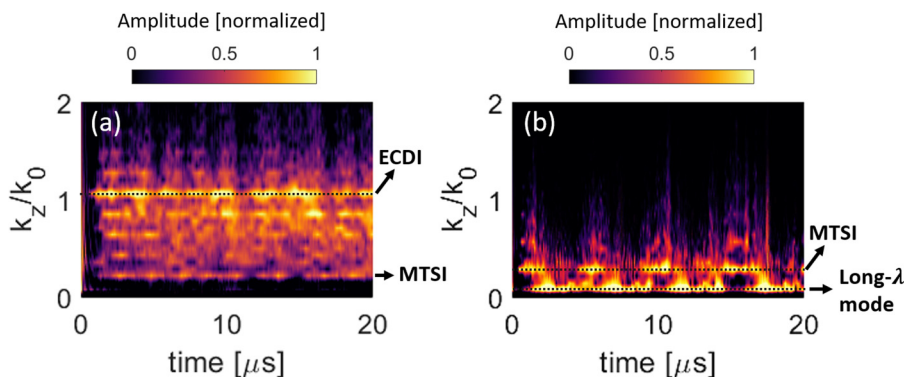


FIG. 6. The time evolution of the 1D spatial FFT of the azimuthal electric field signal within the time interval of 0–20 μs from the simulations of (a) Config. 1 and (b) Config. 3. These plots are obtained following the approach of Ref. 3.

Downloaded from http://pubs.aip.org/jap/article-pdf/doi/10.1063/5.0138223/16788652/123301_1_online.pdf

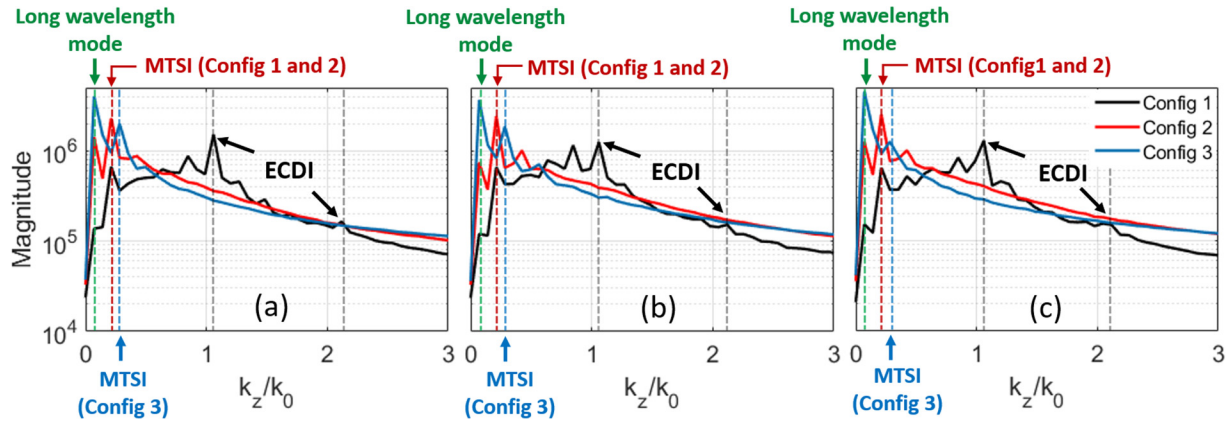


FIG. 7. 1D spatial FFT plots of the azimuthal electric field signal from various B-Config simulations, averaged over all radial positions and over three time intervals: (a) 5–10 μs, (b) 15–20 μs, and (c) 25–30 μs.

occurring at the same $\frac{k_z}{k_0}$ and frequency as those for Config. 1. For Config. 3, the first MTSI harmonic is seen in all time intervals in Fig. 7, but it is slightly shifted to shorter wavelengths compared to Configs. 1 and 2. The frequency of the first MTSI harmonic for Config. 3 is the same as that for Configs. 1 and 2, i.e., 1.2 MHz. The second MTSI harmonic for Config. 3 is only present during the time interval of 15–20 μs in Fig. 7 and is not distinctly evident in Fig. 8.

For the magnetic configurations 2 and 3, we notice, in Fig. 7, a long-wavelength mode at $\frac{k_z}{k_0} \sim 0.07$, which has been also observed in the corresponding 2D snapshots of Fig. 5. The long-λ mode can be easily distinguished in Fig. 8 as well for Config. 3 at the frequency of 0.9 MHz. For this magnetic configuration, this long wavelength mode has the largest magnitude across the spatial and temporal FFT spectra.

The final point to mention concerning the characteristics of the azimuthal instabilities is that we have shown in Fig. 27 of the Appendix that, for Config. 1, the linear dispersion relation of the ion sound waves can be fitted well on the dispersion plot of the wave modes. However, for Configs. 2 and 3, the $\omega - k_z$ spectra of the waves show clear deviation from the linear and nonlinear theoretical dispersion relations of the ion acoustic wave (IAW).

We now assess the effect of the observed instability wave modes on the axial and cross field mobility of the electrons. It should be noted that, in Config. 1, the magnetic field is radially constant and, thus, the axial and cross field mobilities are equivalent. However, in Configs. 2 and 3, due to the radially varying magnetic field profile, the two mobility terms are different. In this regard, the time-averaged electrons' axial mobility, whose radial distribution for the three magnetic configurations is shown in Fig. 9(a), is obtained using the time-averaged axial electrons' velocity (v_{ey}) and the (constant) axial electric field (E_y) as given by Eq. (3). The time-averaged electrons' cross field mobility, whose radial profile is seen in Fig. 9(b), is calculated using Eqs. (4) to (6) and according to the schematic illustrated in Fig. 9(c),

$$\mu_y = \left| \frac{v_{ey}}{E_y} \right|, \tag{3}$$

$$v_{e\perp} = |v_{ey} \cos\theta| + |v_{ex} \sin\theta|, \tag{4}$$

$$E_{\perp} = |E_y \cos\theta| + |E_x \sin\theta|, \tag{5}$$

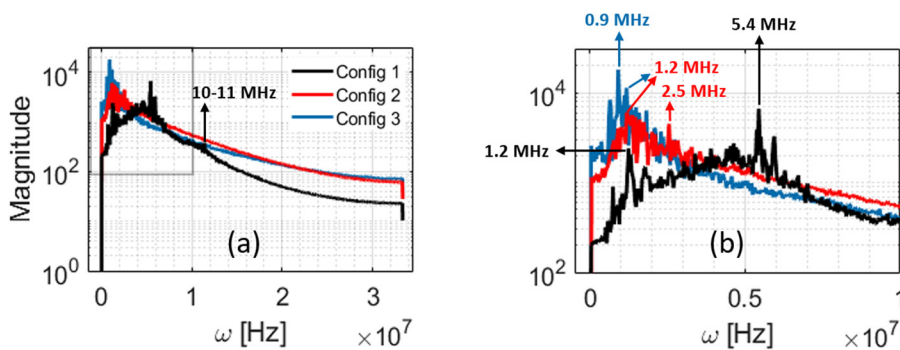


FIG. 8. 1D temporal FFT plots of the azimuthal electric field signal from various B-Config simulations, averaged over all radial positions; (a) spectrum over the frequency range of 0–30 MHz, (b) zoomed-in view of the spectrum in plot (a) over the frequency range of 0–10 MHz.

Downloaded from http://pubs.aip.org/jap/article-pdf/doi/10.1063/5.0138223/16788652/123301_1_online.pdf

$$\mu_{\perp} = \frac{v_{e\perp}}{E_{\perp}}. \tag{6}$$

In Eqs. (4)–(6), $v_{e\perp}$ is the electrons’ cross field velocity, v_{ex} is the electrons’ radial velocity, E_{\perp} is the magnitude of the electric field vector perpendicular to the magnetic field line at each radial location, E_x is the radial electric field component, and μ_{\perp} is the cross field mobility. θ is the angle between the x axis and the tangent to the magnetic field line.

It is observed in Fig. 9(a) that the radially averaged electrons’ axial mobility is the highest for Config. 3, followed by that for Config. 2. The mean μ_y for Config. 1 is much lower than the corresponding values for Configs. 2 and 3. The mean values for the three configurations are expectedly consistent with those observed in Fig. 3(d). The radial profile of μ_y for Config. 2 [Fig. 9(a)] shows sharp increases toward the walls, which is due to the fact that the magnetic field lines in Config. 2 are along the y-direction near the walls [Fig. 1(d)]. Hence, it is also of interest to look at the electrons’ cross field mobility (μ_{\perp}) in Fig. 9(b). As it was expected, the rise in the mobility profile near the walls for Config. 2 is now less significant, and the mean μ_{\perp} for Config. 3 is more distinctly higher than that for Config. 2. Moreover, it is observed in plot (b) of Fig. 9 that the cross field mobility is overall lower in the center of the domain and increases toward the walls before decreasing again. This behavior is more pronounced for Config. 2 in which the time-averaged radial profile of μ_{\perp} also shows an oscillatory distribution, absent in the other two cases.

Considering the results shown in Fig. 9 and noting that, for Config. 3, the long- λ mode was seen to be dominant (Fig. 5, third row, and Fig. 7), it seems that the high cross field mobility in this magnetic configuration is due to the long- λ wave. To verify this speculation and to also identify the main contributor to the electrons’ mobility among various instability modes in the other magnetic configurations, we present in Fig. 10 the time evolution of the electrons’ axial mobility and the amplitude of the dominant azimuthal wave modes ($|E_z|^2$) separately for Configs. 1 to 3 over the time interval of 5–30 μ s.

It is noticed that, for Config. 1 [Fig. 10(a)], the time evolution of μ is in phase with the evolution of the amplitude of the dominant first harmonic of the ECDI, which underlines that the electrons’ axial mobility in this case is mostly driven by the ECDI modes. For Config. 2 [Fig. 10(b)], the fluctuations in μ are of larger amplitude compared to Config. 1 and are instead correlated with the oscillations in the amplitude of first MTSI harmonic, i.e., the dominant MTSI mode for Config. 2 as seen in Fig. 7. Finally, for Config. 3, a rather violent temporal fluctuation in μ is observed in Fig. 10(c), which is correlated with the oscillations in $|E_z|^2$ for the long- λ mode. Indeed, the electrons’ axial mobility is noticed to peak whenever the strong long- λ instability becomes dominant.

Another interesting point from the plots in Fig. 10 is that, for each configuration, the two dominant instability modes seem to interact and exchange energy such that when one mode strengthens, the other weakens. This behavior has been also reported in Ref. 19 for the interactions between ECDI and MTSI in the benchmark’s setup, which is identical to Config. 1 [Fig. 10(a)].

To conclude the discussions in this section, we look at the normalized radial and azimuthal velocity distribution functions for the electrons and the ions at the end of the simulations, i.e., at $t = 30 \mu$ s. The distribution functions are shown in Fig. 11. It is observed in Fig. 11(a) that, for Config. 1, the tail of the electrons’ radial velocity distribution function is lost, whereas the confinement of the plasma in Configs. 2 and 3 has resulted in the retainment of the tail of the distribution functions. Moreover, the radial EVDF for Config. 2 spans across a broader range of velocities, which is consistent with the higher electron temperature observed for this configuration in Fig. 2. Comparing the radial EVDF in plot (a) against the azimuthal one in plot (b) of Fig. 11, the distribution functions for Configs. 2 and 3 seem to be rather isotropic, which is in line with the results of Ref. 16.

Concerning the radial and azimuthal ions’ velocity distribution functions, we notice, from the radial IVDF [Fig. 11(c)], that the distributions increasingly deviate from a Maxwellian from Config. 1 to Config. 3. Especially for Configs. 2 and 3, the IVDFs are depleted in the mid-velocity range, with the depletion being more significant for Config. 3. The azimuthal IVDFs for

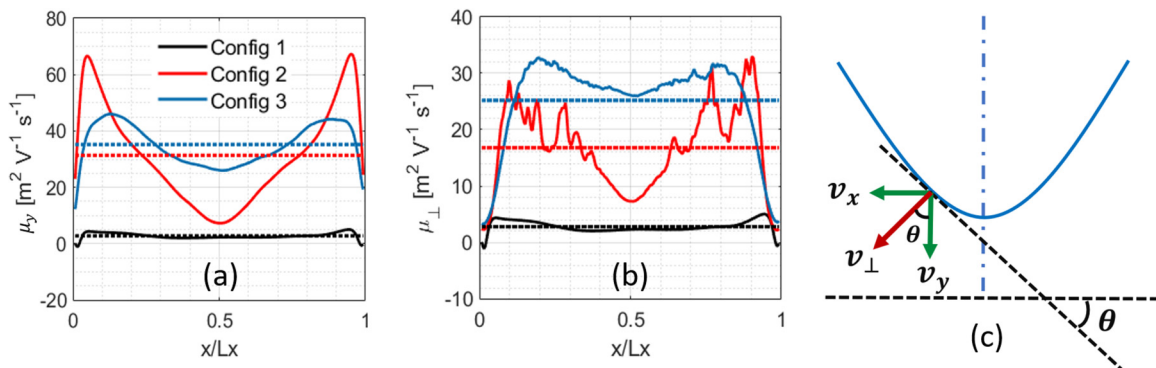


FIG. 9. Comparison between the time-averaged (over 25–30 μ s) radial profiles of (a) electrons’ axial mobility, and (b) electrons’ cross field mobility for various magnetic field configurations. In (c), a schematic associated with the calculation of the cross field velocity is shown; the blue curve represents the magnetic field line.

Downloaded from http://pubs.aip.org/aip/jap/article-pdf/doi/10.1063/5.0138223/16788652/123301_1_online.pdf

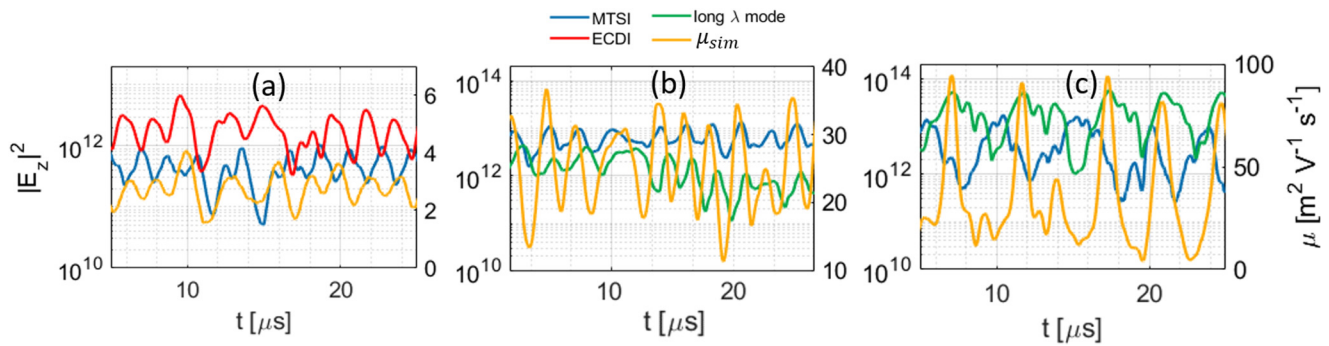


FIG. 10. Time evolution of the amplitude of the dominant azimuthal modes (left axes) and the average electrons' mobility (right axes) for (a) Config. 1, (b) Config. 2, and (c) Config. 3. The approach pursued to plot the time evolution of $|E_z|^2$ for the dominant wave modes identified from the 1D spatial FFTs (Fig. 7) is explained in Ref. 19.

Configs. 2 and 3 [Fig. 11(d)] show a considerable broadening, which is again more pronounced for Config. 3. The distortions of the IVDFs, particularly for Config. 3, suggest a strong interaction between the ions and the long- λ waves, which seems to have caused a redistribution of the ions' energy from the radial direction to the azimuthal one.

B. The effect of secondary electron emission

In this section, we present and discuss the results concerning the effect of the SEE phenomenon on the plasma processes along the radial-azimuthal coordinates.

The SEE from the walls is accounted for using a linear model. A linear SEE model provides a rather simple estimate of the SEE

yield coefficient (γ) according to

$$\gamma(\epsilon) = \min\left(\gamma_{max}, \gamma_0 + \frac{\epsilon}{\epsilon^*}(1 - \gamma_0)\right). \quad (7)$$

In the above equation, ϵ is the primary electron energy, γ_{max} is the maximum electron emission coefficient, γ_0 is the probability of attachment, and ϵ^* is the crossover energy, i.e., the energy at which the SEE yield coefficient becomes equal to 1. For the studies presented in this article, we have kept the values of γ_{max} and γ_0 constant and equal to their corresponding values for Boron Nitride, which are $\gamma_{max} = 2.9$ and $\gamma_0 = 0.578$. However, we have varied the ϵ^* value over a broad range, from 5 to 35 eV. Modifying the crossover energy values implies changing the slope of the linear part of the γ vs energy plot as it is illustrated in Fig. 12.

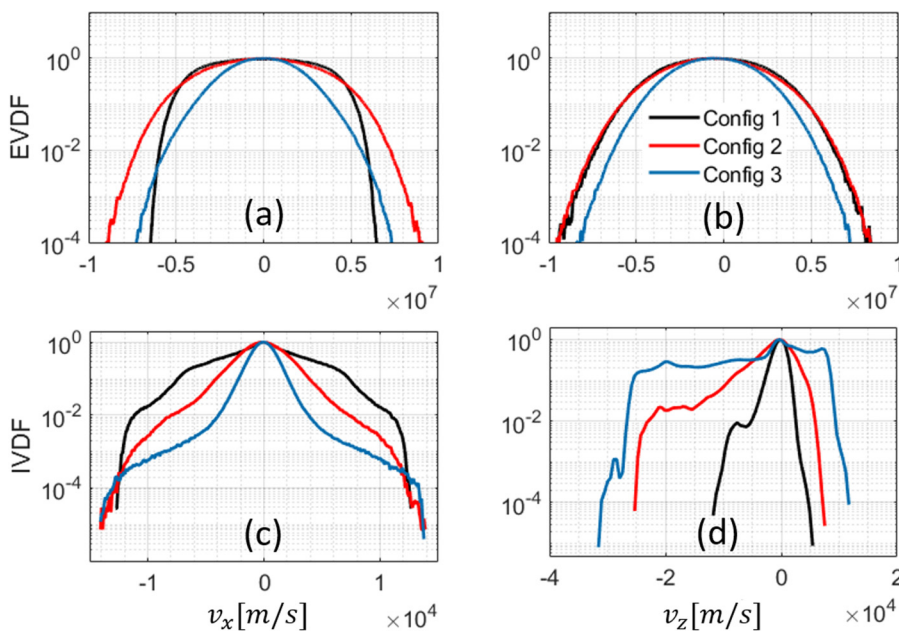


FIG. 11. Normalized radial and azimuthal velocity distribution functions for various magnetic field configurations. First row: electrons' velocity distribution function along (a) the radial (x) and (b) the azimuthal (z) direction; second row: ions' velocity distribution function along (a) the radial and (b) the azimuthal direction.

Downloaded from http://pubs.aip.org/jap/article-pdf/doi/10.1063/5.0138223/16798652/123301_1_online.pdf

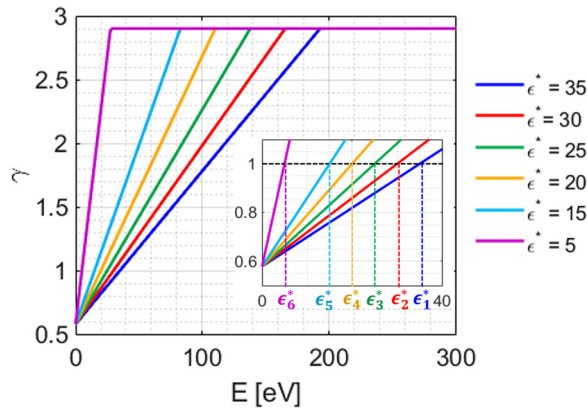


FIG. 12. The variation of the secondary electron emission yield vs the electron energy for various ϵ^* values according to the linear re-emission model.

From plots (a) and (b) in Fig. 13, it is noticed that decreasing the value of ϵ^* results in a consistent increase in the time-averaged ion number density and a decrease in the time-averaged electron temperature. In this regard, Fig. 13(c) shows that the time-averaged SEE yield increases for lower ϵ^* values. Consequently, the higher emission rate of relatively cold secondary electrons reduces T_e . This, in turn, translates into a smaller sheath potential drop for lower ϵ^* , which reduces the radial flux of the ions, hence, increasing the ion number density in the bulk.

It is also interesting to note from Fig. 13(c) that, for $\epsilon^*=5$ eV, the time-averaged γ is slightly below 1. As ϵ^* is increased to 15 eV, γ is stabilized at about the critical SEE yield value for xenon ($\gamma_{cr} = 0.985$), which corresponds to a space-charge saturated sheath. Increasing ϵ^* further results in a monotonic decrease in γ .

Figure 14 presents the 2D snapshots of several plasma parameters from the simulations with various ϵ^* values at an instance of time corresponding to a local maximum in the radial electron temperature. The No-SEE case, i.e., the first column in Fig. 14, corresponds to the benchmark's baseline setup and, as such, the 2D

distributions in this case are representative of the results in Refs. 18 and 19, with the MTSI-like patterns being fully developed. However, as the SEE is taken into account and the value of ϵ^* is reduced from 25 to 5 eV, the overall structures in the 2D snapshots and the values of the plasma properties become notably different. In particular, an increasing cooling effect is clearly visible in the 2D snapshots of the radial electron temperature when the SEE rate becomes more and more significant. Furthermore, a long-wavelength instability mode is seen to become dominant for ϵ^* values of 5 and 15 eV. In this respect, we observe from the plots of E_z and, especially, J_{ey} in Fig. 14 that, by decreasing the crossover energy, the 2D distributions change from that of the No-SEE case with dominant MTSI modes to those of the $\epsilon^*=5$ eV where large-scale, coherent structures have appeared. A video of the cyclic evolution of J_{ey} from the No-SEE simulation case and the simulations with various ϵ^* values is available in Ref. 30.

To analyze more closely the characteristics of the observed wave modes in Fig. 14, we refer to Figs. 15 and 16. Figure 15 shows the average 1D spatial FFTs of the azimuthal electric field from the various- ϵ^* simulations in three time intervals along the simulation, whereas Fig. 16 presents the 1D temporal FFTs of the azimuthal electric field fluctuations over the entire duration of the simulations. From the plots in Figs. 15 and 16, it is evident that for ϵ^* values of 15–35 eV, the first harmonics of the ECDCI and MTSI are clearly present throughout the simulations. However, for ϵ^* equal to 15 and 5 eV, we notice that the long- λ wave is the dominant mode. In addition, in the case of $\epsilon^*=5$ eV, the ECDCI and MTSI modes are not distinctly visible in either the spatial or temporal FFT plots. Indeed, the ECDCI does not appear as a single dominant mode but seems to be present as a spectrum of modes around $\frac{k_z}{k_0}$ of about 1 in Fig. 15 and ω of around 5 MHz in Fig. 16.

The above observations concerning the ECDCI and the MTSI modes are also evident from the time evolution plot of k_z in Fig. 17, where for the case of $\epsilon^*=5$ eV [plot (b)], the MTSI is not observed, the ECDCI appears as a broadband spectrum with a periodic evolution, and the long-wavelength mode is seen to develop in the first few microseconds of the simulation and persists throughout with a constant magnitude. In contrast, we see in plot (a) of Fig. 17 that, for the case of $\epsilon^*=35$ eV, the ECDCI is present as a distinctly

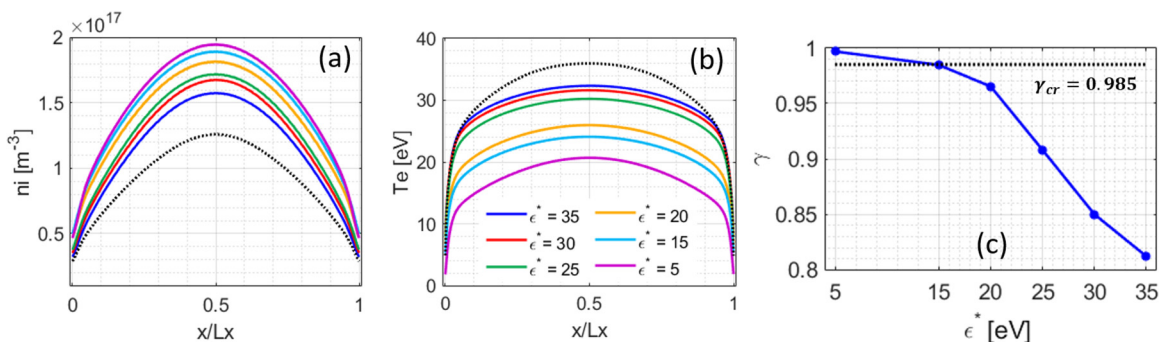


FIG. 13. Time-averaged (over 25–30 μ s) radial profiles of (a) ion number density and (b) electron temperature for various ϵ^* values. Plot (c) shows the variation vs ϵ^* of the SEE yield, i.e., the ratio of the secondary emitted to primary electrons, averaged over the entire simulation duration.

Downloaded from http://pubs.aip.org/aip/jap/article-pdf/doi/10.1063/5.0138223/16788652/123301_1_online.pdf

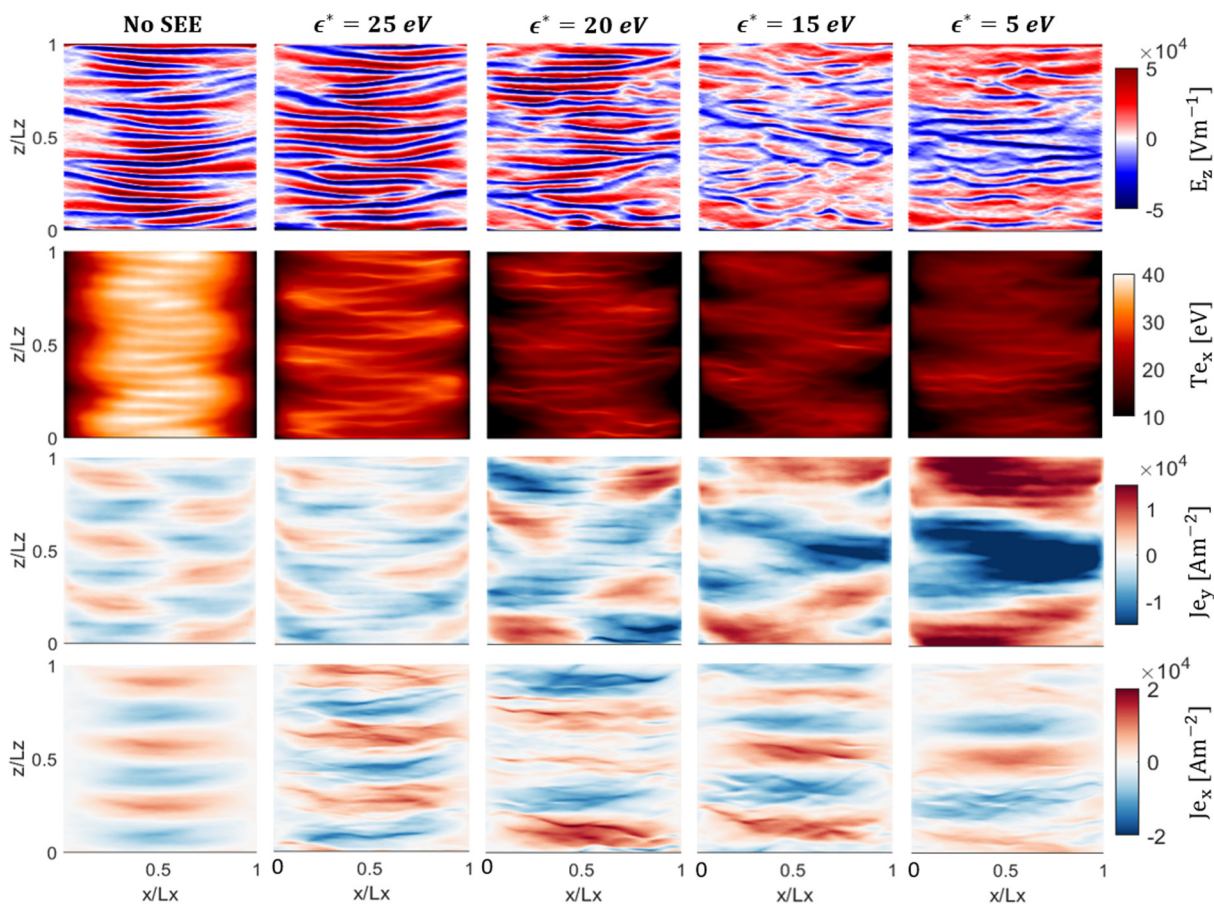


FIG. 14. Comparison between the 2D snapshots of several plasma properties at the time of local maximum of radial electron temperature from the simulations with various ϵ^* against a simulation with no SEE. The rows, from top to bottom, represent the azimuthal electric field, radial electron temperature, and the axial and radial current densities, respectively.

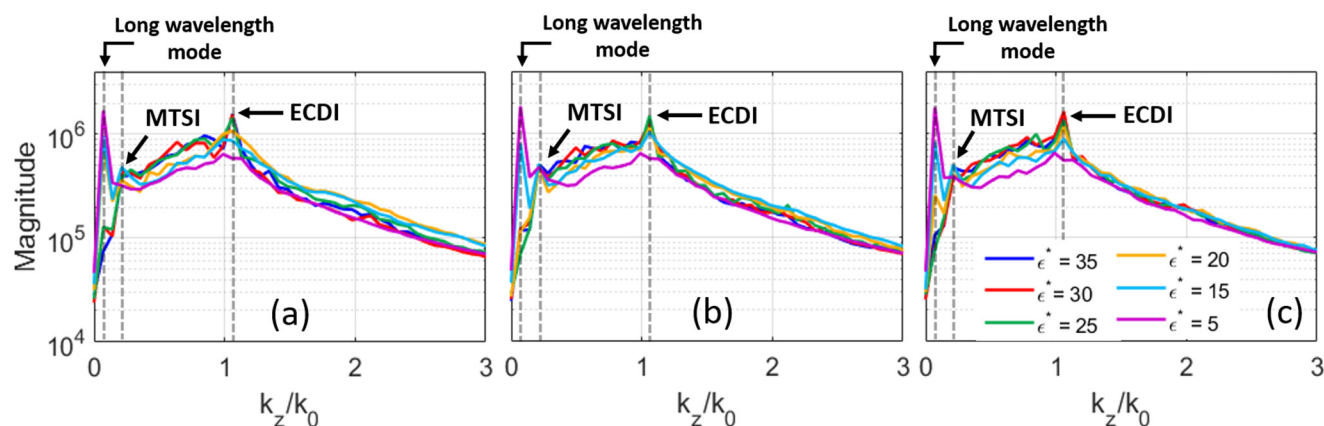


FIG. 15. 1D spatial FFT plots of the azimuthal electric field signal from the simulations with various ϵ^* , averaged over all radial positions and over the time intervals of (a) 5–10 μs , (b) 15–20 μs , and (c) 25–30 μs .

Downloaded from http://pubs.aip.org/jap/article-pdf/doi/10.1063/5.0138223/16788652/123301_1_online.pdf

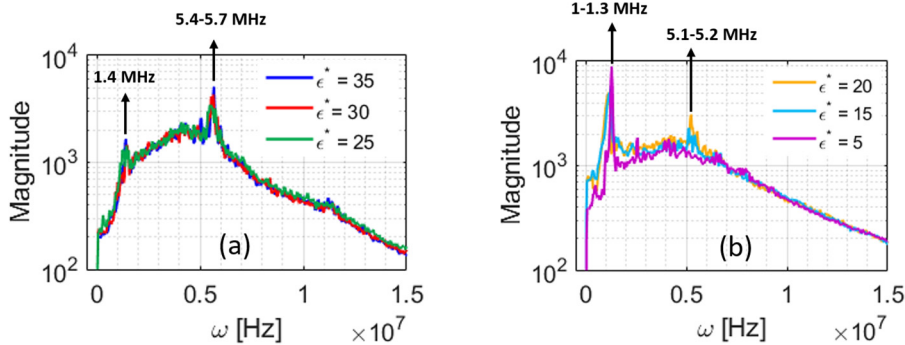


FIG. 16. 1D temporal FFT plots of the azimuthal electric field signal from the simulations with various ϵ^* , averaged over all radial positions; (a) ϵ^* values of 35, 30, and 25 eV, (b) ϵ^* values of 20, 15, and 5 eV.

dominant mode and the MTSI is also present even though its magnitude is relatively mitigated compared to that observed from the benchmark's No-SEE case in Fig. 6(a).

It is highlighted that the underlying mechanisms behind the observations concerning the instabilities' characteristics and evolution in the case of $\epsilon^*=5$ eV are not studied here and require further investigation, which is left for future work.

The comparison shown in Fig. 28 of the Appendix between the dispersion plots of the azimuthal waves from various- ϵ^* simulations and the theoretical dispersion relations of the ion acoustic waves revealed that, for ϵ^* values of 25–35 eV, the spectra can be well fitted with the linear dispersion of the ion sound waves. However, from ϵ^* of 20–5 eV, the numerical dispersions increasingly deviate from the dispersion relation of the ion sound waves. In particular, for the case of $\epsilon^*=5$ eV, the dispersion plot is characterized by a broadband spectrum around the frequency and wavenumber of the ECDI with a few distinct modes aligned at an angle with respect to the linear IAW dispersion.

The absence of the MTSI and the smeared ECDI modes in the simulation case of $\epsilon^*=5$ eV are seen in Fig. 18(a) to have resulted in a reduction in the electrons' axial mobility, both in the center of the domain ($\mu_{sim, center}$) and over the total radial extent (μ_{sim}), contrary to the overall trend of the μ vs ϵ^* plot. In fact, it is observed in Fig. 18(a) that, as the crossover energy is reduced, the total mobility and the mobility in the center of the domain increase. This trend is also evident from Fig. 18(b) which shows the time-averaged radial distribution of the electrons' mobility for various ϵ^* values. However, for $\epsilon^*=5$ eV, whereas the difference between

$\mu_{sim, center}$ and μ_{sim} , which implies the significance of the near-wall transport from the SEE, has increased compared to other cases, both mobility terms are lower than the corresponding values for $\epsilon^*=15$ eV.

It is also worth pointing out that the increase in the near-wall mobility for decreasing values of crossover energy, observed in both plots (a) and (b) of Fig. 18, is consistent with the previous results reported in the literature on the effect of the SEE on the electrons' transport.⁶

As the final point on the SEE effects, we have plotted, in Fig. 19, the normalized energy distribution function of the electrons from the simulations with various ϵ^* at $t=30 \mu s$. It is evident from this figure that, as the SEE increases for lower crossover energies, the width of the distributions diminishes. This is because of the cooling effect of the secondary electrons, which was also reflected in the time-averaged profiles of the electron temperature [Fig. 13(b)] for various values of ϵ^* . Accordingly, we see in Fig. 19 that the tail of the distributions become increasingly depleted from the No-SEE case to the case with $\epsilon^*=5$ eV.

C. The effect of plasma number density

The last effect we have studied in this work is that of the plasma number density or, equivalently, the axial ion current density. Since the simulations feature an imposed ionization source, as described in Sec. III, the plasma number density is controlled by the value of the peak of this source. As a result, to investigate the

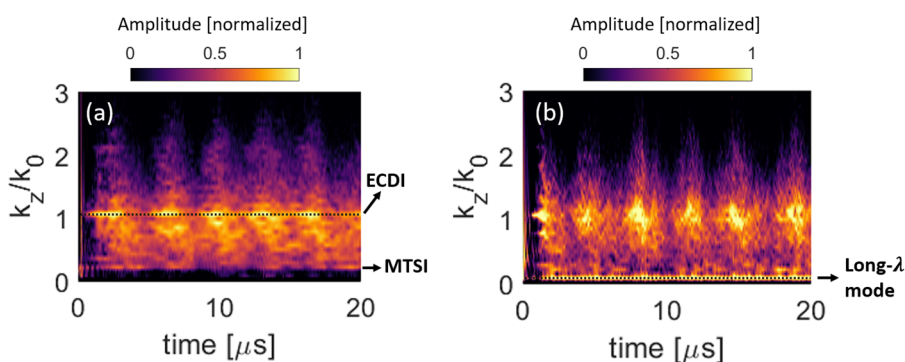


FIG. 17. The time evolution of the 1D spatial FFT of the azimuthal electric field signal within the time interval of 0–20 μs from the simulations with (a) $\epsilon^*=35$ eV, and (b) $\epsilon^*=5$ eV. These plots are obtained following the approach of Ref. 3.

Downloaded from http://pubs.aip.org/jap/article-pdf/doi/10.1063/5.0138223/16788652/123301_1_online.pdf

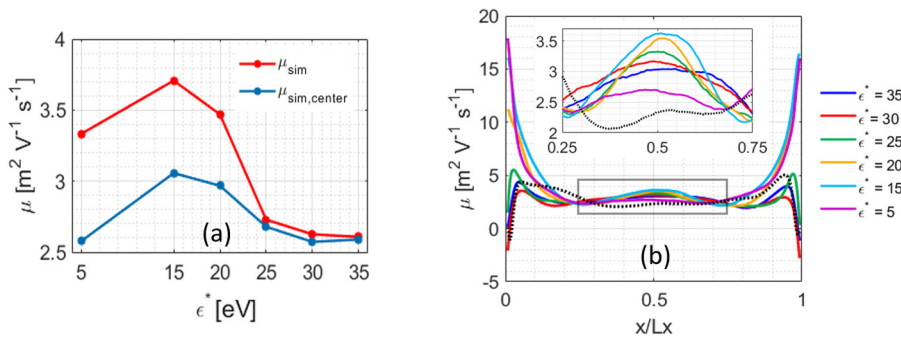


FIG. 18. (a) Variation vs ϵ^* of the electrons' axial mobility terms, μ_{sim} and $\mu_{sim,center}$, averaged over the entire simulation domain and over time; (b) time-averaged (over 25–30 μ s) radial profiles of the electrons' axial mobility for various ϵ^* values. The mobility terms μ_{sim} and $\mu_{sim,center}$ are both calculated using Eq. (2), but for $\mu_{sim,center}$, only electrons within the range of 0.25 to 0.75 x/L_x are considered. The dashed black line in plot (b) corresponds to the no-SEE case.

effect of plasma number density, we have changed the nominal peak of the ionization source, S_0 , by a factor ranging from $\frac{1}{32}$ to 6.

In this regard, Fig. 20 presents the radial distributions of the ion number density and the electron temperature for various peak values of the ionization source (S). Expectedly, as the peak of the ionization source is increased, so does the ion number density [Fig. 20(a)]. The increase in the ion (plasma) number density can also translate into stronger wave-particle interactions,²⁴ which, in turn, causes a more significant heating of the plasma by the azimuthal instabilities and, thus, increasing higher electron temperatures. This trend is clearly observed in the time-averaged electron temperature profiles in Fig. 20(b).

The increase in the plasma number density also affects the azimuthal wave content of the discharge, and the overall associated magnitudes of the excited wave modes. This is illustrated in Figs. 21 and 22, which show, respectively, the 1D spatial and temporal FFT plots of the azimuthal electric field signal from the simulations with various values of S . From Fig. 21, in particular, we can distinguish three distinct plasma regimes depending on the plasma number density, or the value of S .

In the first regime, from $\frac{S_0}{32}$ to $\frac{S_0}{8}$, the ECDI does not exist whereas the first harmonic of the MTSI is visible. The second harmonic of the MTSI is also excited for $S = \frac{S_0}{16}$ and $\frac{S_0}{8}$, which is more

distinctly visible in Fig. 21. From Fig. 22, the frequency of first MTSI harmonic is seen to be in the range of 1–1.8 MHz across the simulations with S values from $\frac{S_0}{32}$ to $\frac{S_0}{8}$.

In the second regime, for S in the range of $\frac{S_0}{4}$ to S_0 , the first and second harmonics of the MTSI, as well as the first harmonic of the ECDI are noticed in Fig. 21. In the nominal case, the second ECDI harmonic at $\frac{k_z}{k_0}$ slightly higher than 2 and with the frequency of about 11 MHz is also visible.

In the third regime, i.e., for $3S_0$ and $6S_0$, the ECDI mode is not observed as a single mode but rather as a continuous spectrum around the wavenumber associated with this instability. Moreover, the long- λ mode and the first harmonic of the MTSI are visible in both the spatial and temporal FFT plots. In the case of $S = 3S_0$, the second MTSI harmonic can be also seen in the time intervals of 5–10 μ s and 25–30 μ s in Fig. 21. The presence of the second MTSI harmonic in the case of $S = 3S_0$, which induces further heating of the electrons, can justify a slightly higher time-averaged T_e for this case in Fig. 20(b) compared to the case with $S = 6S_0$.

In Fig. 23, we have shown the temporal evolution of the normalized azimuthal wavenumber of the electric field fluctuations from the simulations with $3S_0$ and $6S_0$. In line with the observations pointed out regarding Figs. 21 and 22, we notice from Fig. 23 as well that, in both simulation cases, the wavenumber spectrum is quite broadband. Moreover, in the case of $S = 6S_0$ [Fig. 23(b)], the broadband spectrum of the wave modes features a periodic temporal variation in time. At this plasma density, it is interesting to note that the long- λ mode is formed earlier into the simulation compared to the lower-density simulation with $S = 3S_0$.

As the last point concerning the waves' spectra from simulations with different plasma densities, the plots in Fig. 29 of the Appendix illustrated that the numerical dispersion of the azimuthal wave modes is only consistent with the linear dispersion of the IAW for the simulations with S in the range of $\frac{S_0}{4}$ to S_0 , i.e., in the second plasma regime identified above.

Moving on to the effect of the plasma number density on the electrons' axial mobility, we observe, in Fig. 24(a), that, as the plasma density increases, the spatiotemporally averaged electrons' mobility monotonically increases. This is an expected behavior since the FFT plots in Fig. 21 illustrated that the overall intensity of the excited wave modes increases with the plasma number density and, additionally, the electron-wave interactions are more significant at a higher plasma density.

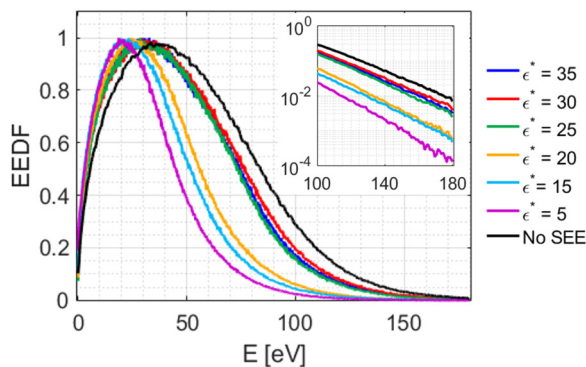


FIG. 19. Normalized electrons' energy distribution function for various ϵ^* values. The zoomed-in view on the tail of the EEDF is also shown where the x axis is in a logarithmic scale.

Downloaded from http://pubs.aip.org/jap/article-pdf/doi/10.1063/5.0138223/16798652/123301_1_online.pdf

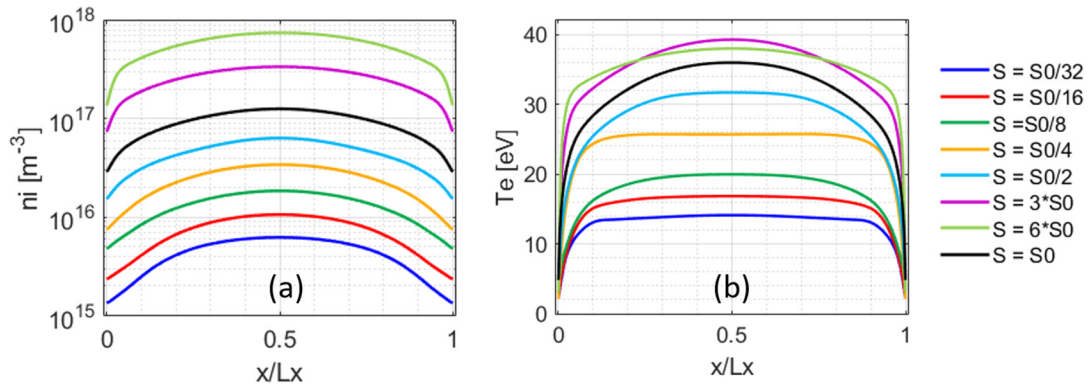


FIG. 20. Time-averaged (over 25–30 μ s) radial profiles of (a) ion number density, and (b) electron temperature from the simulations with various ionization source peak intensities (S).

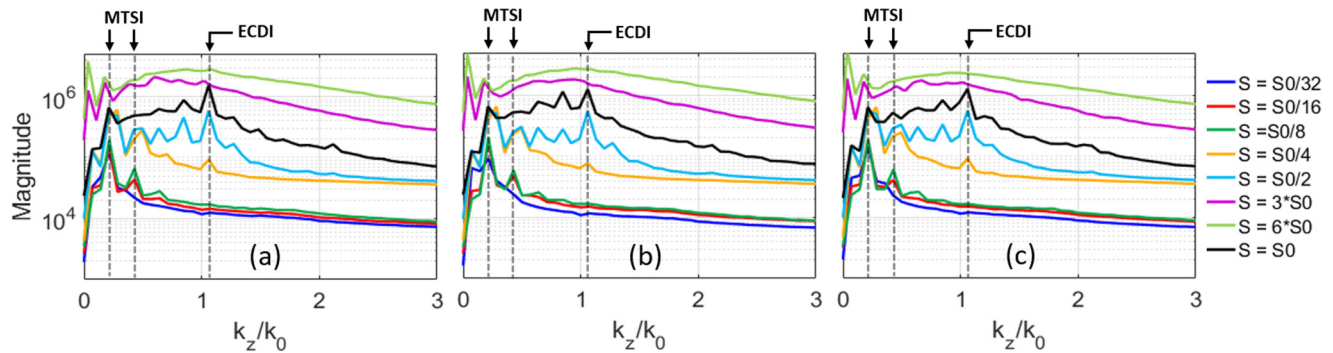


FIG. 21. 1D spatial FFT plots of the azimuthal electric field signal from the simulations with various S , averaged over all radial positions and over the time intervals of (a) 5–10 μ s, (b) 15–20 μ s, and (c) 25–30 μ s.

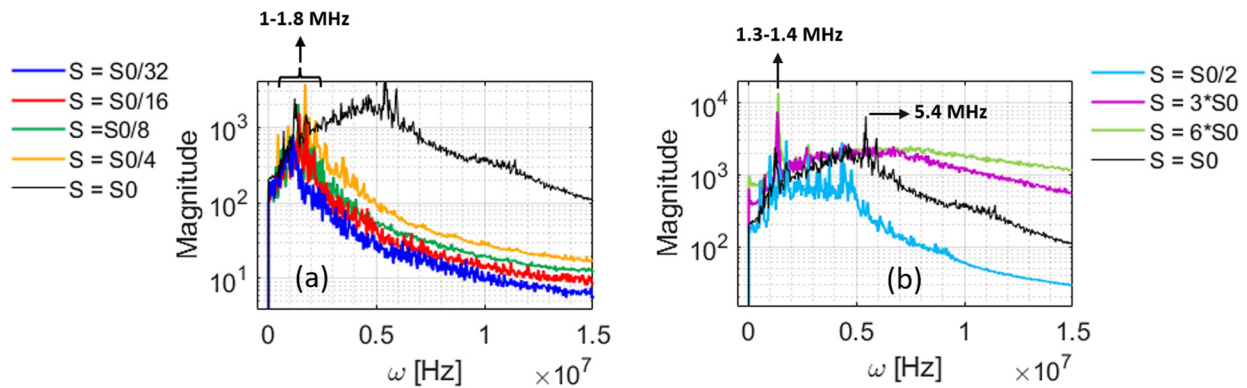


FIG. 22. 1D temporal FFT plots of the azimuthal electric field signal from the simulations with various S , averaged over all radial positions; (a) S values in the range of $[S_0/32, S_0/4]$, (b) S values in the range of $[S_0/2, 6S_0]$. The frequency spectrum corresponding to the benchmark case with $S = S_0$ is shown for reference on both plots.

Downloaded from http://pubs.aip.org/jap/article-pdf/doi/10.1063/5.0138223/16788652/123301_1_online.pdf

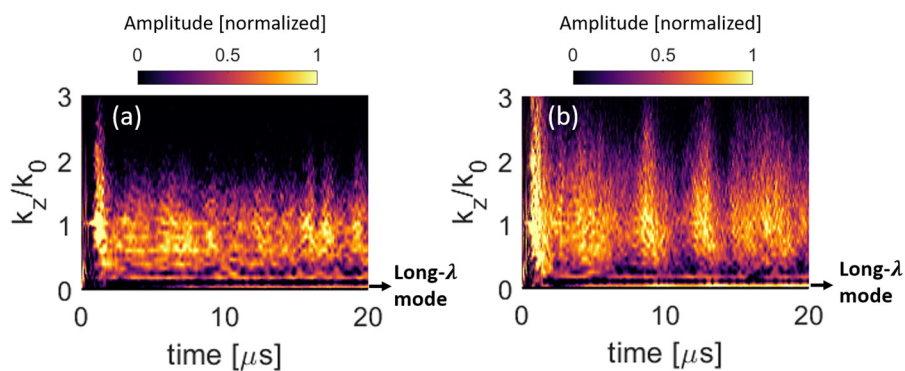


FIG. 23. The time evolution of the 1D spatial FFT of the azimuthal electric field signal within the time interval of 0–20 μ s from the simulations with (a) $S = 3S_0$ and (b) $S = 6S_0$. These plots are obtained following the approach of Ref. 3.

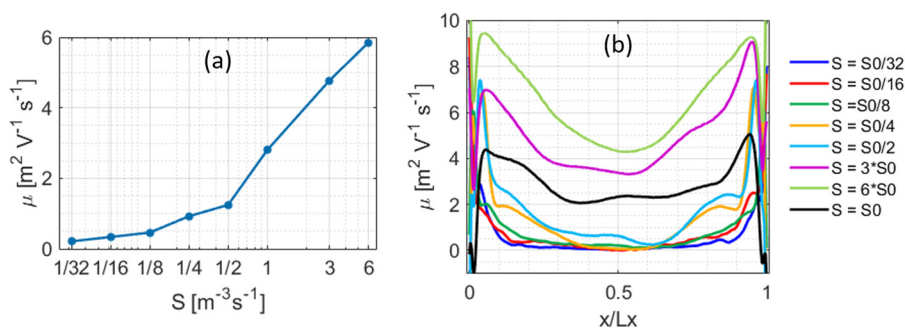


FIG. 24. (a) Variation vs S of the electrons' axial mobility averaged over the entire simulation domain and over time, (b) the time-averaged (over 25–30 μ s) radial profiles of the electrons' axial mobility for various values of S .

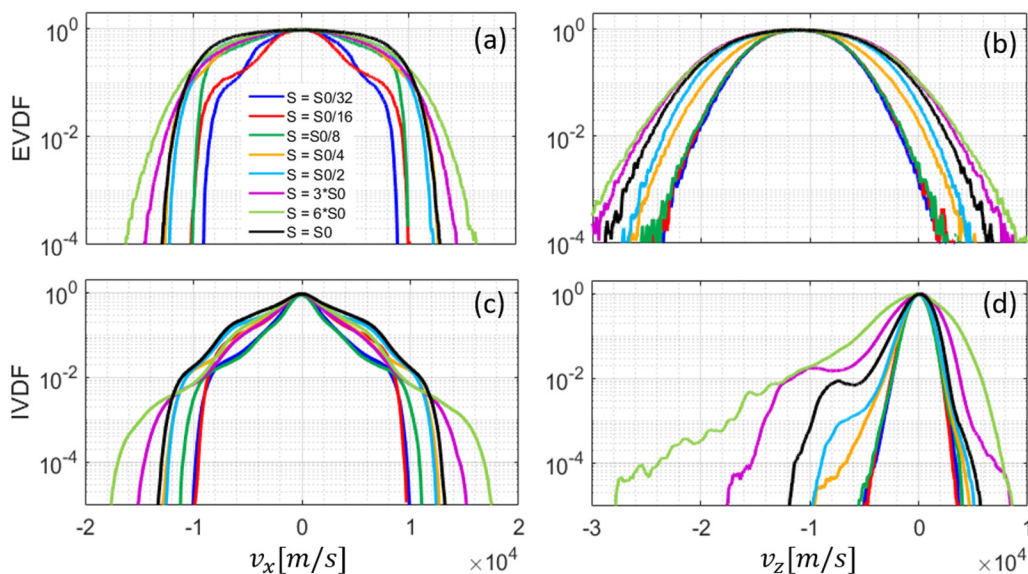


FIG. 25. Normalized particles' velocity distribution functions for various values of S . First row: electrons' velocity distribution functions along (a) radial and (b) azimuthal direction; second row: ions' velocity distribution functions along (a) radial and (b) azimuthal direction.

Downloaded from http://pubs.aip.org/jap/article-pdf/doi/10.1063/5.0138223/16788652/123301_1_online.pdf

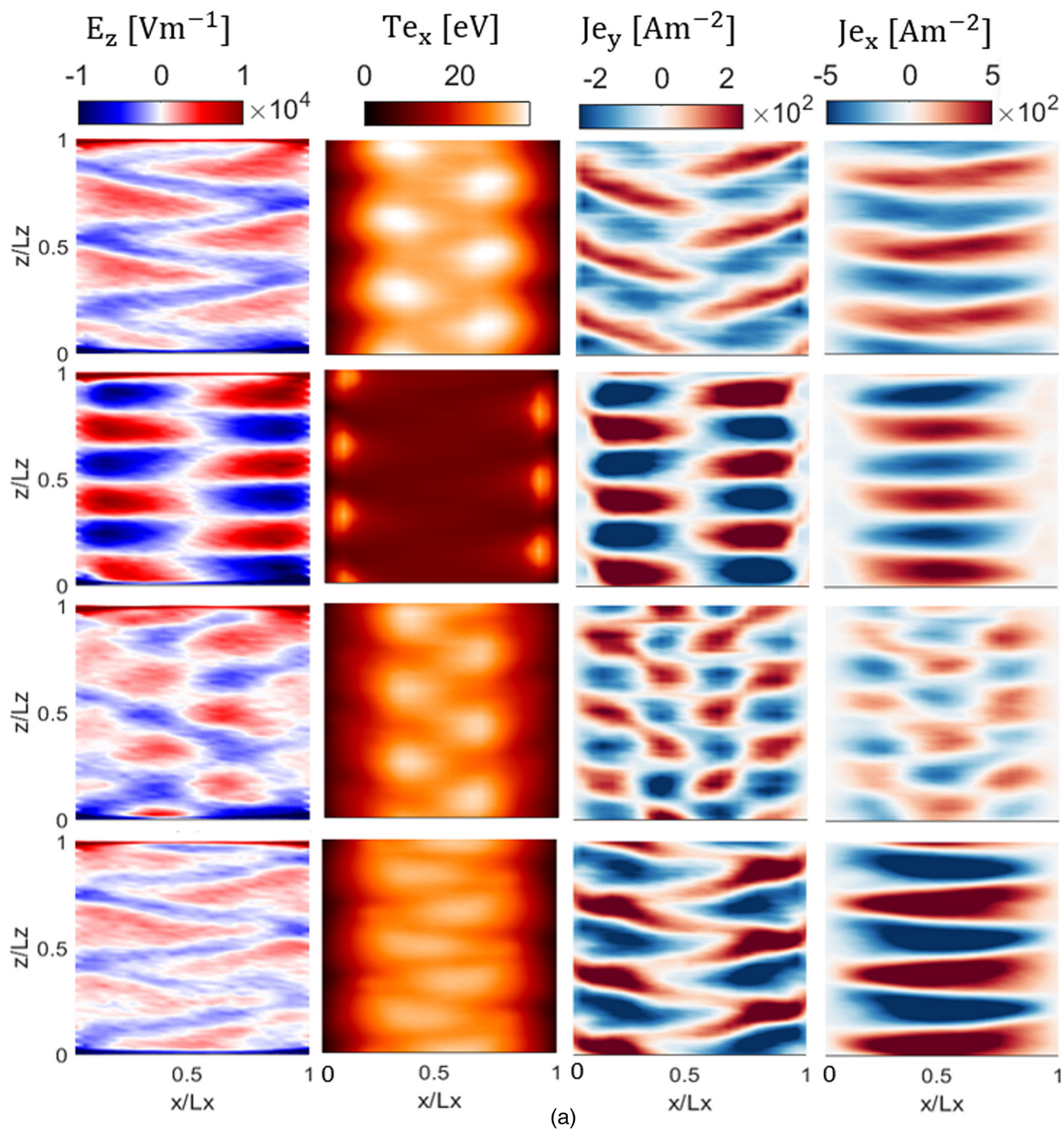

 Downloaded from http://pubs.aip.org/jap/article-pdf/doi/10.1063/5.0138223/16788652/123301_1_online.pdf

FIG. 26. 2D snapshots of the plasma properties through one evolution cycle of the discharge from the simulations with (a) $S = S_0/16$, (b) $S = S_0/8$, (c) $S = 3S_0$, and (d) $S = 6S_0$. In each subplot, the columns, from left to right, represent the azimuthal electric field, radial electron temperature, and the axial and radial electron current densities, respectively. Also, the rows, from top to bottom, represent various instances in one period (T) of the discharge evolution, i.e., t_0 and T , $t_0 + \frac{T}{4}$, $t_0 + \frac{T}{2}$, $t_0 + \frac{3T}{4}$.

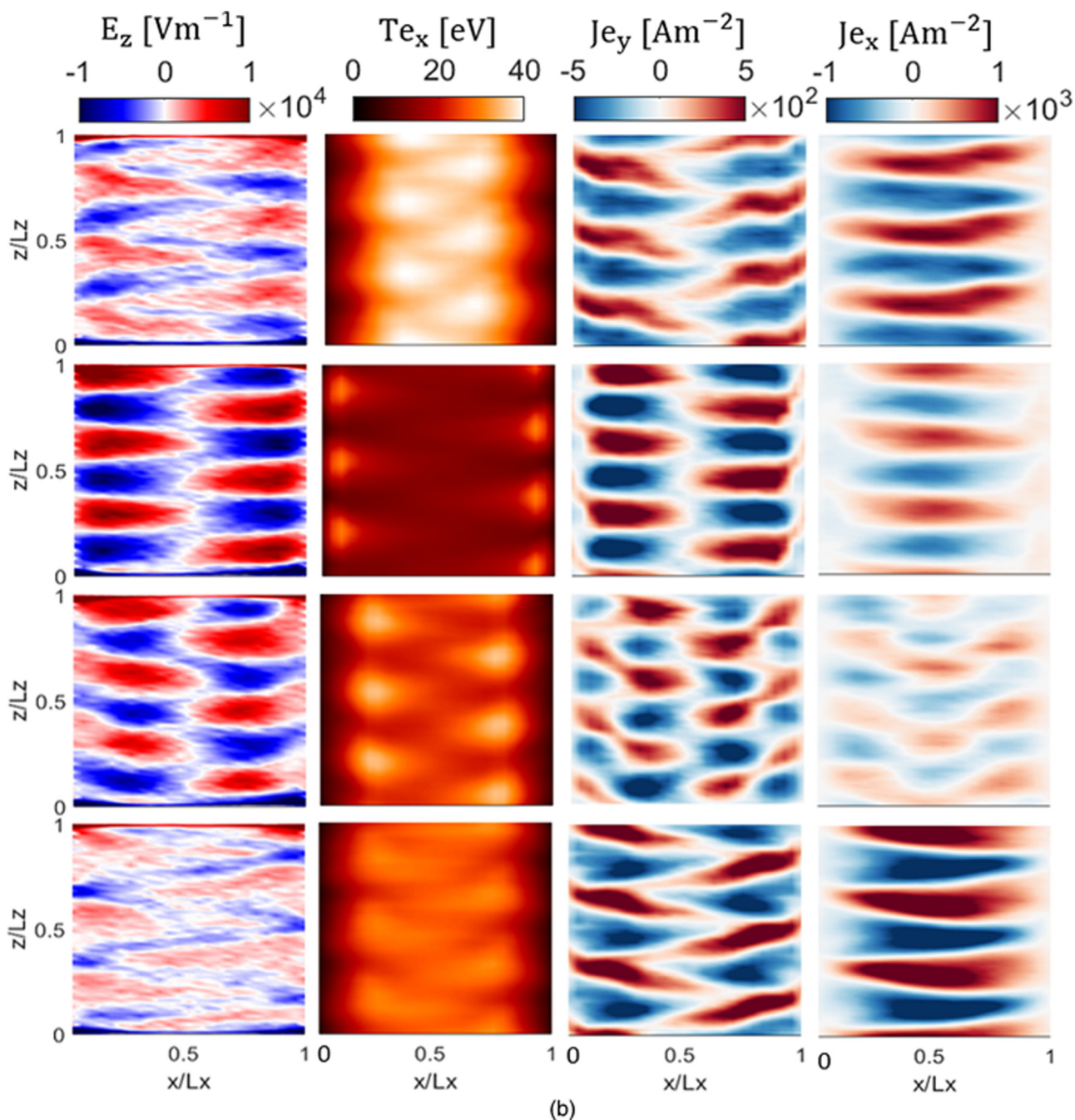
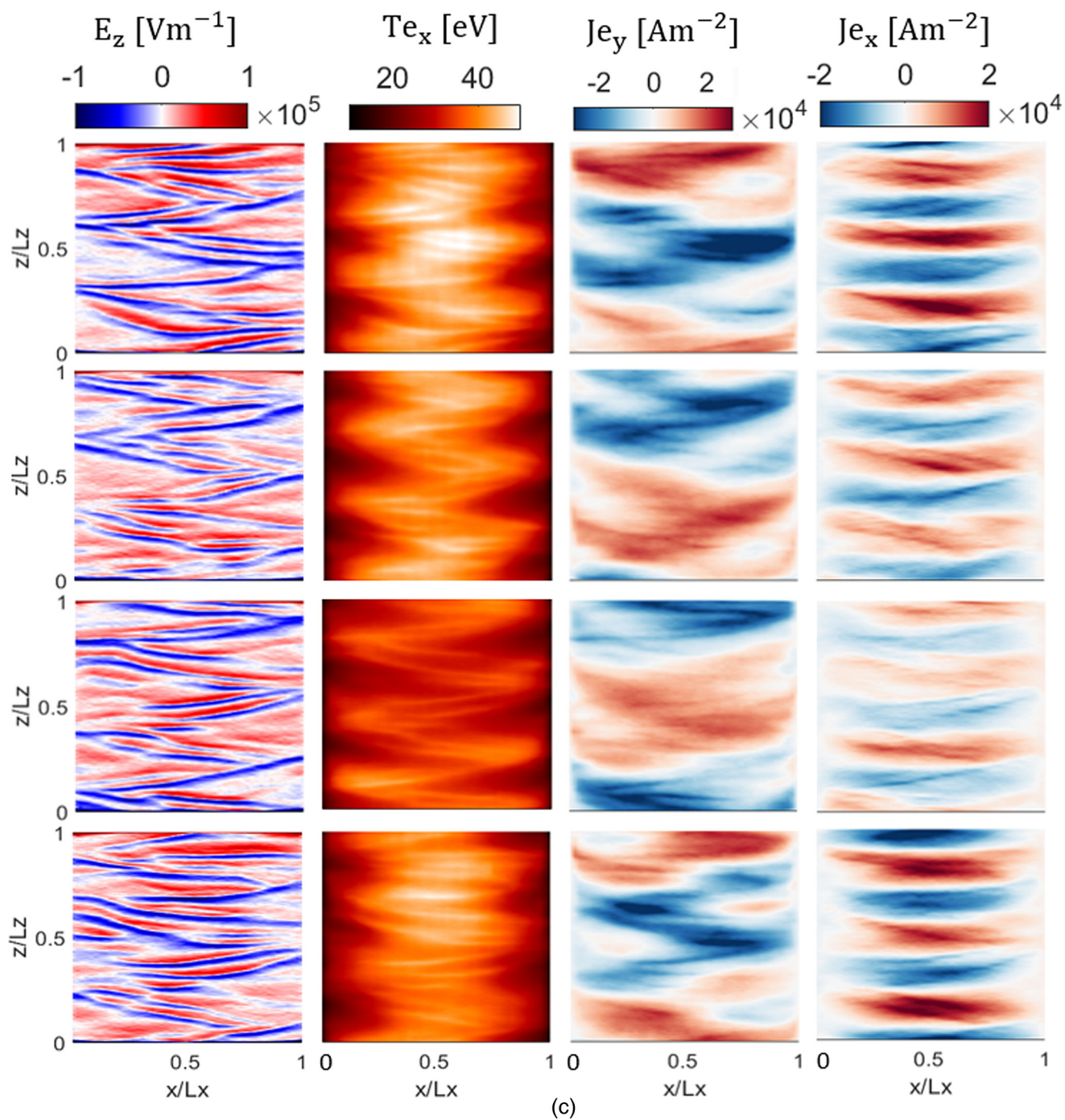


FIG. 26. (Continued.)

The trend mentioned above between the electrons' mobility and the plasma number density can be also noticed from the time-averaged radial distributions of the electrons' mobility in Fig. 24(b). Referring to this figure, it is interesting to note that, for cases with

S in the range of $\frac{S_0}{32}$ to $\frac{S_0}{2}$, the mobility around the center of the domain, i.e., $\frac{x}{L_x} \sim 0.5$, is quite similar. However, as the spectrum of the excited azimuthal instabilities changes from the very low number density cases to those corresponding to S values of $\frac{S_0}{4}$ and

Downloaded from http://pubs.aip.org/jap/article-pdf/doi/10.1063/5.0138223/16788652/123301_1_online.pdf

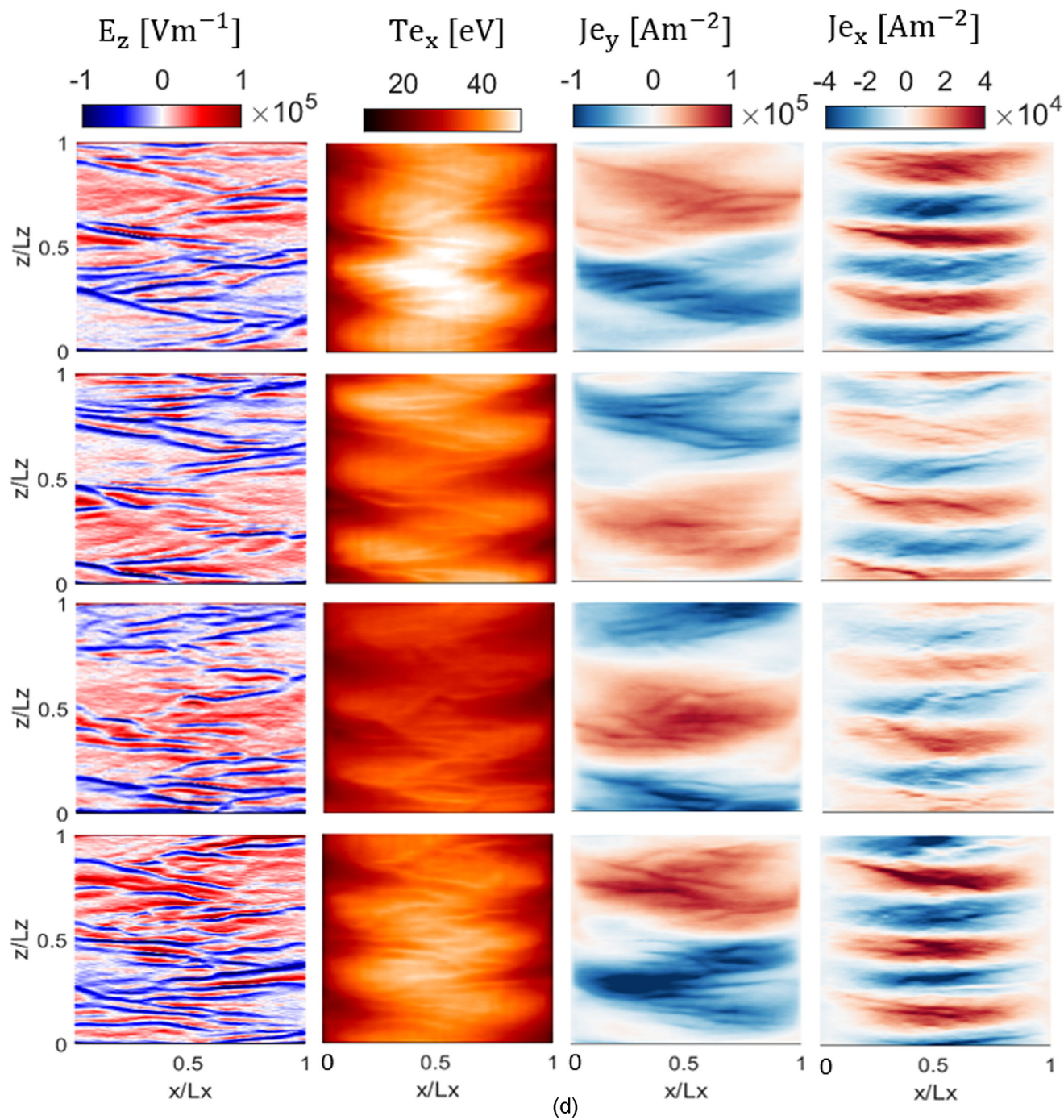


Downloaded from http://pubs.aip.org/jap/article-pdf/doi/10.1063/5.0138223/16788652/123301_1_online.pdf

FIG. 26. (Continued.)

$\frac{S_0}{2}$, the mobility profiles show a more notable increase from the center of the domain toward the walls. For the nominal case with $S = S_0$, the mobility in the bulk is higher than the cases with $\frac{S_0}{4}$ and $\frac{S_0}{2}$, but it is lower near the walls. In the cases with S value of

$3S_0$ and $6S_0$, as the long- λ mode becomes more dominant with increasing plasma density, the radial profile of the electrons' mobility overall moves toward larger values both in the bulk and near the walls.



Downloaded from http://pubs.aip.org/jap/article-pdf/doi/10.1063/5.0138223/16788652/123301_1_online.pdf

FIG. 26. (Continued.)

The normalized velocity distribution functions of the ions and electrons along the radial and azimuthal directions are provided in Fig. 25 for the simulations with various S values at $t = 30 \mu\text{s}$. From plot (a) in Fig. 25 corresponding to the electrons' radial VDF, we

observe that, as the plasma density increases, the radial EVDF is increasingly broadened and moves toward a Maxwellian. The azimuthal EVDF [Fig. 25(b)] shows an increasing heating of the electrons along the azimuth for higher plasma densities. These two

observations are consistent with the fact that higher plasma number densities translate into stronger azimuthal waves and more significant interactions between the plasma species and the instabilities.

In this respect, the radial and azimuthal IVDFs, Figs. 25(c) and 25(d), also exhibit clear signs of the heating of the ion population along both directions. This heating is most significant for the cases with $S = 3S_0$ and $6S_0$, where the long- λ mode was seen to develop and become dominant.

Finally, in Fig. 26, we have compared the 2D snapshots of various plasma properties through one evolution cycle of the discharge from the simulations corresponding to low and high plasma-number-density limits, namely, $S = \frac{S_0}{16}$ and $S = \frac{S_0}{8}$ vs $S = 3S_0$ and $S = 6S_0$. It is overall noticed that the visualizations in Fig. 26 are consistent with the 1D FFT plots shown in Fig. 21.

Looking more closely at the different subplots in Fig. 26 and the plots within, we notice that, in the cases with low plasma density, only MTSI-like structures are present. However, as the discharge evolves in one cycle, the first harmonic of the MTSI becomes dominant at $t = t_0 + \frac{T}{4}$, following by the dominance of the second harmonic at $t_0 + \frac{T}{2}$. The interactions between these MTSI harmonics causes a merging and splitting of the modes, leading to the tilted structures observable at $t = t_0$ and $t_0 + \frac{3T}{4}$.

In the high number density limit, on the contrary, the 2D plasma distributions are dominated by the long-wavelength mode superimposed on a spectrum of shorter wavelength ECDI and MTSI waves. The long- λ wave mode is seen to be always dominantly present, but its amplitude slightly varies over the discharge's evolution cycle. A video of the dynamics of the discharge in terms of the time evolution of the axial electron current density (J_{ey}) from the simulations with various plasma number densities is available in Ref. 31.

The development of the long- λ mode in the case of $S = 3S_0$ [Fig. 26(c)] and the similar plasma number density in this case [Fig. 20(a)] compared to the simulation in Sec. IV B with an SEE level corresponding to $\epsilon^* = 5$ eV [Fig. 13(a)], for which the same long-wavelength mode was observed, allows us to link the observations and conclude that the formation of this mode is mainly driven by the plasma number density. Nevertheless, it is pointed out that the azimuthal wave content is case dependent and varies depending on the plasma conditions.

V. CONCLUSIONS

In this article, we presented the results of an extensive parametric study in an $E \times B$ plasma configuration representative of a radial-azimuthal section of a Hall thruster. The studies were focused on the effects of three physical factors on the characteristics and the dynamics of the azimuthal instabilities and the consequent wave-induced electron transport in this 2D configuration. The numerous kinetic simulations whose results were discussed in this work were carried out using the reduced-order IPPL-Q2D PIC code at an order of approximation of the 2D problem corresponding to 50 regions along either the radial or azimuthal direction. The cost-effectiveness of the 50-region quasi-2D simulation, which was demonstrated in Ref. 18, and the

interesting insights derived from this effort confirm the power of the reduced-order PIC code to be readily used as a tool for the verification of the theoretical predictions and/or to derive new theories to explain the nature of the physical phenomena of interest based on a more comprehensive set of observations regarding their variations over a wide range of plasma conditions. This is a desired capability that the significant computational cost of the traditional fully multi-dimensional PIC codes had so far hindered achieving.

The physical factors whose influence we investigated in this paper were the radial gradient in the magnetic field, the secondary electron emission, and the plasma number density. The common finding from all of the simulations performed was that, in cases where the plasma density in the central part of the domain away from the walls is elevated due to any of the studied factors, a long-wavelength wave mode with the frequency of about 1 MHz develops. Even though the exact effect of this wave mode on the plasma species differs among the studied cases and depends on the conditions of the plasma, it overall causes a notable axial mobility of the electrons and a heating of the ion population.

To summarize the main effects observed from each of the specific physical factors, we demonstrated that the gradients in the magnetic field configuration affect the spectrum of the azimuthal instabilities, which consequently changes the dominant mechanism behind the electrons' axial mobility. In this regard, it was shown that in the case of a uniform radial magnetic field profile, i.e., the benchmark setup, the main contributor to transport was the ECDI. In contrast, for a simulation configuration representative of a cross section of magnetically shielded Hall thrusters inside the discharge channel, we observed that the MTSI plays a dominant role in the electrons' transport. In addition, for a configuration representative of the near-plume of the shielded thrusters, the long- λ mode was seen to play the major role in the electrons' axial mobility. In this same configuration, we showed that the formation of the long- λ wave mode was due to an inverse energy cascade of the shorter wavelength modified two-stream instability. To the best of our knowledge, this is the first time that the 2D radial-azimuthal physics of the Hall thrusters with a shielding magnetic field topology is being studied using high-fidelity kinetic simulations.

Concerning the effect of the SEE, we showed that decreasing the value of the crossover energy leads to a consistent increase in the near-wall mobility. However, since the azimuthal wave content and the dominant instability modes were seen to vary as well with the strength of the SEE phenomenon, the variation of the overall average mobility vs ϵ^* did not show an always monotonic behavior and decreased for the lowest crossover energy value studied ($\epsilon^* = 5$ eV), potentially due to the absence of the MTSI and the smeared ECDI modes in this case. For $\epsilon^* = 5$ eV, the long- λ mode was shown to develop early into the simulation and to persist as the dominant wave mode, coexisting with a broadband spectrum of ECDI modes.

Increasing the plasma number density was seen to translate into stronger azimuthal waves and a more significant broadening of the plasma species' velocity distribution functions. Accordingly, we observed a monotonically increasing average

electrons' axial mobility with the plasma density and an increasing ion heating along the radial and azimuthal directions, with the ions' azimuthal velocity distribution function showing a notable asymmetry at the highest plasma densities studied. Moreover, increasing the plasma number density was shown to modify the azimuthal wave content. In this respect, for cases with the lowest plasma densities, only the MTSI modes were seen to be present. Whereas, at the highest plasma densities, the long- λ mode was noticed to coexist with a broadband spectrum of shorter-wavelength wave modes.

For each physical factor, we carried out a comparison between the numerical dispersion of the observed azimuthal instabilities from the simulations and the nonlinear dispersion relation of the ion acoustic waves as well as their linearized dispersion ($\omega = k_z C_s$). This analysis was performed to assess the variation in the dispersion features of the azimuthal modes due to the physical factors investigated. The dispersion analyses did not lead to a definitive, generally applicable conclusion. However, the following main observations were made: (1) for the simulation cases with a non-uniform radial distribution of the magnetic field, the spectra of the waves showed clear deviations from the linear and nonlinear theoretical dispersion relations of the ion acoustic waves; (2) in the presence of the SEE, the linear dispersion relation of the ion acoustic waves was only fitting the dispersion map of the instabilities for $\epsilon^* \geq 25$ eV; (3) across the simulation cases with varying plasma number density, the spectra of the azimuthal wave modes were observed to coincide with the linear ion acoustic dispersion relation only in the plasma regime where the first and second harmonics of the MTSI in addition to the first harmonic of the ECDI were present.

Finally, regarding the long-wavelength mode reported in this article, it is pointed out that, in the simulation of B-Config. 3 in Sec. IV A and in the simulations of Sec. IV C with the peak ionization source values of $3S_0$ and $6S_0$, we captured half a wavelength of the wave along the azimuthal direction. This suggests that, in these simulation cases, the long- λ wave mode was limited by the size of the simulation box along the azimuth. Nevertheless, we emphasize that our intention in this effort was to maintain the simulation setup as similar as possible to that of the benchmark¹⁹ so as to be able to assess the variations in the observed physics from the benchmarking activity due to various physical factors. Hence, we kept the same azimuthal domain length as that of the benchmark for our parametric studies. In this regard, even though a similar azimuthal length to the one we used here had been chosen in previous literature as well to study the instabilities and the inverse energy cascade in the radial-azimuthal configuration,^{3,7} the influence that the domain length along the azimuth may have had on the characteristics and the effects of the long- λ mode warrants further study in a future work.

ACKNOWLEDGMENTS

The present research is carried out within the framework of the project "Advanced Space Propulsion for Innovative Realization of space Exploration (ASPIRE)." ASPIRE has received funding from the European Union's Horizon 2020 Innovation Programme

under Grant Agreement No. 101004366. The views expressed herein can in no way be taken as to reflect an official opinion of the Commission of the European Union. The authors also acknowledge the computational resources and support provided by the Imperial College Research Computing Service (<http://doi.org/10.14469/hpc/2232>).

AUTHOR DECLARATIONS

Conflict of Interest

The authors have no competing interests to declare that are relevant to the content of this article.

Author Contributions

M. Reza: Conceptualization (equal); Formal analysis (equal); Methodology (equal); Software (equal); Visualization (lead); Writing – original draft (lead). **F. Faraji:** Conceptualization (equal); Formal analysis (equal); Methodology (equal); Software (equal); Visualization (supporting); Writing – review & editing (equal). **A. Knoll:** Conceptualization (equal); Project administration (lead); Supervision (lead); Writing – review & editing (equal).

DATA AVAILABILITY

The data that support the findings of this study are available from the corresponding author upon reasonable request.

APPENDIX: DISPERSION PLOTS OF THE AZIMUTHAL ELECTRIC FIELD FLUCTUATIONS

Figures 27–29 show the numerical dispersion plots of the azimuthal electric field fluctuations in the $\omega - k_z$ plane from the simulations with, respectively, various radial magnetic field profiles, different values of the crossover energy (ϵ^*), and varying peak values of the ionization source (S) or, equivalently, the plasma density. For reference, the dispersion relation of the ion acoustic waves in the ions' reference frame,²⁵ given by Eq. (A1), is superimposed as yellow curves on all plots. In Eq. (A1), C_s is the ion sound speed and λ_D is the Debye length,

$$\omega \approx \frac{k_z C_s}{\sqrt{1 + k_z^2 \lambda_D^2}}. \quad (\text{A1})$$

Moreover, following the same analysis pursued in Ref. 7, we have plotted as dashed red lines in Figs. 27–29 the linear dispersion relation of the ion sound waves, Eq. (A2), which corresponds to the relation in Eq. (8) in the limit of the azimuthal wavenumber being much larger than the Debye length, i.e., $k_z \lambda_D \ll 1$,

$$\omega \approx k_z C_s. \quad (\text{A2})$$

The discussion of the plots shown here is presented within the main text of this article. In particular, Fig. 27 is referred to in Sec. IV A and Fig. 28 is discussed in Sec. IV B. The discussion of the plots in Fig. 29 is provided in Sec. IV C.

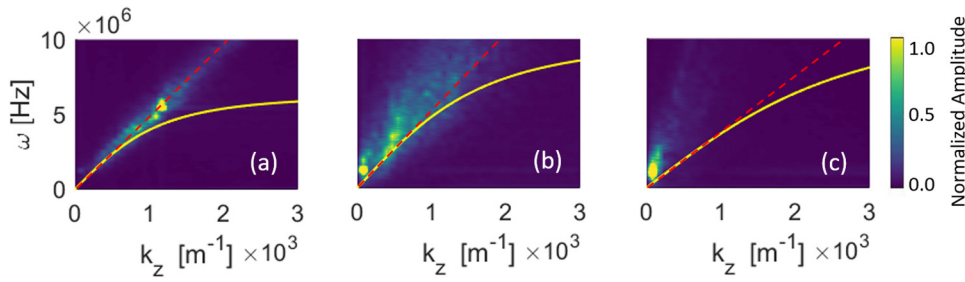


FIG. 27. Dispersion plots of the azimuthal electric field fluctuations at the mid-radial location from various B-Config simulations: (a) Config. 1, (b) Config 2, (3) Config 3. The theoretical dispersion relations of the ion acoustic waves, Eqs. (A1) and (A2), calculated using the time-averaged plasma properties at the mid-radial location are superimposed on each plot.

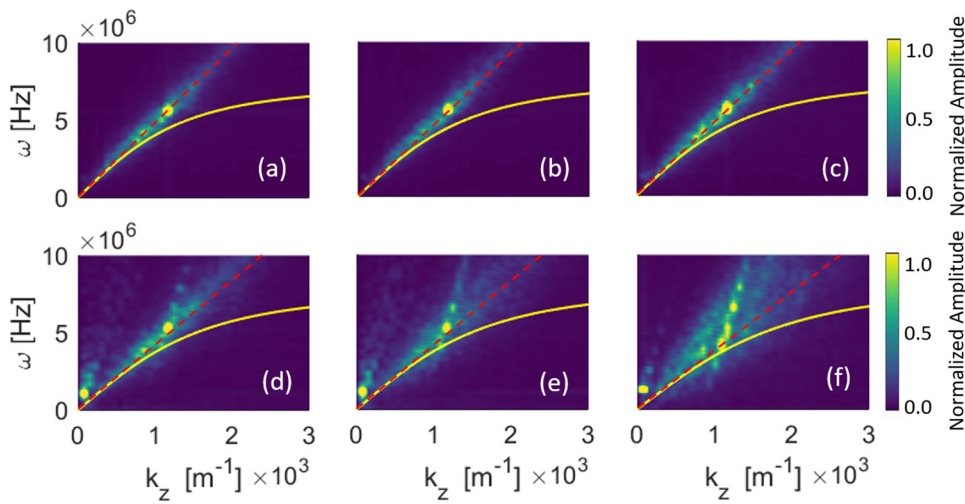


FIG. 28. Dispersion plots of the azimuthal electric field fluctuations at the mid-radial location from the simulations with various ϵ^* values: (a) 35 eV, (b) 30 eV, (c) 25 eV, (d) 20 eV, (e) 15 eV, (f) 5 eV. The theoretical dispersion relations of the ion acoustic waves, Eqs. (A1) and (A2), calculated using the time-averaged plasma properties at the mid-radial location are superimposed on each plot.

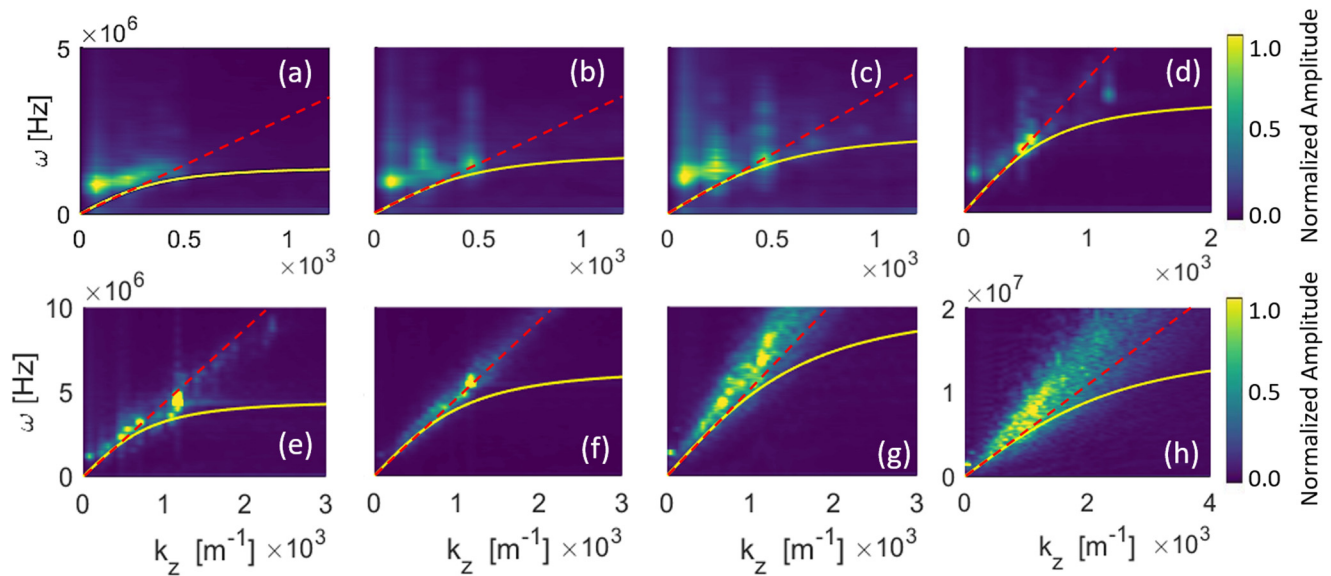


FIG. 29. Dispersion plots of the azimuthal electric field fluctuations at the mid-radial location from the simulations with various S values: (a) $S_0/32$, (b) $S_0/16$, (c) $S_0/8$, (d) $S_0/4$, (e) $S_0/2$, (f) S_0 , (g) $3S_0$, (h) $6S_0$. The theoretical dispersion relations of the ion acoustic waves, Eqs. (A1) and (A2), calculated using the time-averaged plasma properties at the mid-radial location are superimposed on each plot.

Downloaded from http://pubs.aip.org/aip/jap/article-pdf/doi/10.1063/5.0138223/16788652/123301_1_online.pdf

REFERENCES

- ¹J. P. Boeuf, "Tutorial: Physics and modeling of Hall thrusters," *J. Appl. Phys.* **121**, 011101 (2017).
- ²I. D. Kaganovich, A. Smolyakov, Y. Raitses *et al.*, "Physics of E×B discharges relevant to plasma propulsion and similar technologies," *Phys. Plasmas* **27**, 120601 (2020).
- ³S. Janhunen, A. Smolyakov, D. Sydorenko, M. Jimenez, I. Kaganovich, and Y. Raitses, "Evolution of the electron cyclotron drift instability in two dimensions," *Phys. Plasmas* **25**, 082308 (2018).
- ⁴V. Croes, T. Lafleur, Z. Bonaventura, A. Bourdon, and P. Chabert, "2D particle-in-cell simulations of the electron drift instability and associated anomalous electron transport in Hall-effect thrusters," *Plasma Sources Sci. Technol.* **26**, 034001 (2017).
- ⁵A. Héron and J. C. Adam, "Anomalous conductivity in Hall thrusters: Effects of the non-linear coupling of the electron-cyclotron drift instability with secondary electron emission of the walls," *Phys. Plasmas* **20**, 082313 (2013).
- ⁶A. Tavant, V. Croes, R. Lucken, T. Lafleur, A. Bourdon, and P. Chabert, "The effects of secondary electron emission on plasma sheath characteristics and electron transport in an E×B discharge via kinetic simulations," *Plasma Sources Sci. Technol.* **27**, 124001 (2018).
- ⁷F. Petronio, A. Tavant, T. Charoy, A. Alvarez-Laguna, A. Bourdon, and P. Chabert, "Conditions of appearance and dynamics of the modified two-stream instability in E×B discharges," *Phys. Plasmas* **28**, 043504 (2021).
- ⁸F. Taccogna, S. Longo, and M. Capitelli, "Plasma-surface interaction model with secondary electron emission effects," *Phys. Plasmas* **11**(3), 1220–1228 (2004).
- ⁹D. Sydorenko, A. Smolyakov, I. Kaganovich, and Y. Raitses, "Modification of electron velocity distribution in bounded plasmas by secondary electron emission," *IEEE Trans. Plasma Sci.* **34**(3), 815–824 (2006).
- ¹⁰D. Sydorenko, A. Smolyakov, I. Kaganovich, and Y. Raitses, "Kinetic simulation of secondary electron emission effects in Hall thrusters," *Phys. Plasmas* **13**, 014501 (2006).
- ¹¹Y. Raitses, I. D. Kaganovich, A. Khrabrov, D. Sydorenko, N. J. Fisch, and A. Smolyakov, "Effect of secondary electron emission on electron cross-field current in E × B discharges," *IEEE Trans. Plasma Sci.* **39**, 995 (2011).
- ¹²F. Taccogna, S. Longo, M. Capitelli, and R. Schneider, "Anomalous transport induced by sheath instability in Hall effect thrusters," *Appl. Phys. Lett.* **94**, 251502 (2009).
- ¹³I. G. Mikellides, I. Katz, R. R. Hofer, and D. M. Goebel, "Magnetic shielding of a laboratory Hall thruster. I.: Theory and validation," *J. Appl. Phys.* **115**, 043303 (2014).
- ¹⁴I. G. Mikellides and A. Lopez-Ortega, "Growth of the modified two-stream instability in the plume of a magnetically shielded Hall thruster," *Phys. Plasmas* **27**, 100701 (2020).
- ¹⁵J. B. McBride, E. Ott, J. P. Boris, and J. H. Orens, "Theory and simulation of turbulent heating by the modified two-stream instability," *Phys. Fluids* **15**, 2367 (1972).
- ¹⁶A. Marin-Cebrián, A. Domínguez-Vázquez, P. Fajardo, and E. Ahedo, "Kinetic plasma dynamics in a radial model of a Hall thruster with a curved magnetic field," *Plasma Sources Sci. Technol.* **31**, 115003 (2022).
- ¹⁷M. Reza, F. Faraji, and A. Knoll, "Generalized reduced-order particle-in-cell scheme for Hall thruster modeling: concept and in-depth verification in the axial-azimuthal configuration," *J. Phys. D: Appl. Phys.* **56**, 17520 (2022).
- ¹⁸F. Faraji, M. Reza, and A. Knoll, "Verification of the generalized reduced-order particle-in-cell scheme in a radial-azimuthal E×B plasma configuration," *AIP Advances* **13**, 025315 (2023).
- ¹⁹W. Villafana, F. Petronio, A. C. Denig, M. J. Jimenez *et al.*, "2D radial-azimuthal particle-in-cell benchmark for E×B discharges," *Plasma Sources Sci. Technol.* **30**, 075002 (2021).
- ²⁰S. P. Gary and J. J. Sanderson, "Longitudinal waves in a perpendicular collisionless plasma shock: I.: Cold ions," *J. Plasma Phys.* **4**(4), 739–751 (1970).
- ²¹A. Ducrocq, J. C. Adam, A. Héron, and G. Laval, "High-frequency electron drift instability in the cross-field configuration of Hall thrusters," *Phys. Plasmas* **13**, 102111 (2006).
- ²²O. Bunemano, "Instability of electrons streaming through ions across a magnetic field," *J. Nucl. Energy. Part C, Plasma Phys. Accelerators, Thermonuclear Res.* **4**, 111 (1962).
- ²³S. Janhunen, A. Smolyakov, O. Chapurin, D. Sydorenko, I. Kaganovich, and Y. Raitses, "Nonlinear structures and anomalous transport in partially magnetized E×B plasmas," *Phys. Plasmas* **25**, 011608 (2018).
- ²⁴F. Faraji, M. Reza, and A. Knoll, "Enhancing one-dimensional particle-in-cell simulations to self-consistently resolve instability-induced electron transport in Hall thrusters," *J. Appl. Phys.* **131**, 193302 (2022).
- ²⁵M. Reza, F. Faraji, and A. Knoll, "Resolving multi-dimensional plasma phenomena in Hall thrusters using the reduced-order particle-in-cell scheme," *J. Electric Propuls.* **1**, 19 (2022).
- ²⁶T. Lafleur, S. D. Baalrud, and P. Chabert, "Theory for the anomalous electron transport in Hall effect thrusters. I.: Insights from particle-in-cell simulations," *Phys. Plasmas* **23**, 053502 (2016).
- ²⁷A. Domínguez-Vázquez, F. Taccogna, and E. Ahedo, "Particle modeling of radial electron dynamics in a controlled discharge on a Hall thruster," *Plasma Sources Sci. Technol.* **27**, 064006 (2018).
- ²⁸M. Reza, E. Ferrato, F. Faraji, T. Andreucci, and M. Andreucci, "Magnetic circuit optimization for Hall thrusters design," in *Proceedings of the 36th International Electric Propulsion Conference*, Vienna, 15–20 September 2019. Vienna (2019).
- ²⁹See <https://youtu.be/6pNBodDFpRQ> for the video of the simulation results corresponding to Fig. 5 of the article.
- ³⁰See https://youtu.be/D3P26ZC_5z8 for the video of the electrons' axial current density evolution corresponding to Fig. 14 of the article.
- ³¹See <https://youtu.be/PBeX9WL3nkM> for the video of the electrons' axial current density evolution corresponding to Fig. 26 of the article.